A robust virtual element method framework coupling phase-field and cohesive zone models for crack propagation in composite structures

Shubham Sharma, Ananth Ramaswamy*

Department of Civil Engineering, Indian Institute of Science, Bengaluru, Karnataka 560012, India

Abstract

We propose a Virtual Element Method (VEM) framework that couples linear cohesive elements with lowest-order virtual elements to simulate the interplay between matrix cracking and interfacial delamination in composite structures. The matrix domain is discretized using virtual elements based on a phase-field brittle fracture model, enabling accurate representation of crack kinking, curving, and branching. Interfaces are discretized using cohesive elements derived from a potential-based cohesive zone model to capture mixed-mode separation. This coupled discretization handles rapid mesh transitions along interfaces and allows inclusions to be modeled as single polygonal elements with a large number of edges, offering significant meshing flexibility. We validate the framework through numerical examples encompassing mixed-mode interfacial debonding, matrix cracking, crack penetration and deflection at interfaces, and crack kinking from interfaces, comparing results against existing numerical and experimental data. Additionally, we demonstrate a hybrid strategy where the virtual elements are used to discretize inclusions while the finite elements are used to discretize a 3D-printed hyperelastic matrix domain. This hybrid discretization is then employed to simulate multiple crack nucleation and crack coalescence in a 3D-printed hyperelastic composite undergoing finite deformation before brittle fracture. The VEM framework is implemented in the commercial finite element software ABAQUS (Standard) via user-defined elements, making advanced virtual element capabilities accessible within an industry-standard platform. This approach thus provides a robust and flexible tool for simulating brittle fracture in composites with complex damage mechanisms.

Keywords: Virtual element method (VEM), Phase-field fracture, Cohesive Zone Model, Mesh transitions, Polygonal elements

1. Introduction

Composite materials are widely employed in aerospace structures, automotive components, biomedical implants, and civil infrastructure due to their high strength-to-weight

*Corresponding author

Email address: ananth@iisc.ac.in (Ananth Ramaswamy)

ratios. Advancements in the additive manufacturing technology have also led to the development of tailored composites with varying spatial distributions of inclusions to enhance the fracture toughness [52, 83, 105]. Despite these advantages, the inherent heterogeneity of composites makes them prone to complex damage mechanisms such as matrix cracking, fiber breakage, fiber–matrix debonding, crack kinking out of interface, and interlaminar delamination. Consequently, the accurate and robust prediction of crack initiation and propagation in composite structures remains a central challenge in computational mechanics.

Various computational fracture models exist in the literature for modeling the fracture of composite structures [21]. Some popular approaches which have been applied in modeling fracture of composite materials include Continuum Damage Mechanics (CDM) [30, 113, 108, 56, 9, 22], Discrete Element Method (DEM) [60, 53, 84, 48, 26, 29], Cohesive Zone Model (CZM) [57, 104, 32, 6, 31, 2, 5, 41], Extended Finite Element Method (XFEM) [116, 97, 13, 115, 28, 44, 89] amongst others. Typically, a combination of these two damage models is used in simulating fracture in composites to obtain interfacial as well as bulk fracture. In general, the CZM is combined either with CDM or XFEM. CZM is used for modeling interfacial failure while CDM or XFEM is used for modeling bulk failure. Though CZM can properly capture interfacial failure, the use of CDM or XFEM in modeling bulk failure has certain limitations. Since CDM has no regularization parameter, the crack patterns can be mesh-sensitive, while XFEM cannot properly deal with multiple cracks, requires complex crack tracking algorithms for 3D crack propagation problems and can lead to convergence issues [102, 21]. These issues can be eliminated when CZM is used in conjunction with Phase-Field Models (PFM) [64, 7].

There is a growing body of literature directed towards the use of PFM and CZM for simulating fracture in composites [75, 40, 94, 4, 103, 95, 16, 111, 66, 96, 54, 70]. However, all these works use finite elements for discretizing the domain. The problem with using finite elements in a PF + CZM framework is that the elements need to be conforming across the interface boundaries. This can lead to inefficient discretization when the inclusion is rigid, or is of a complex shape. Sometimes, interfaces are not sharp but of finite thickness (also called interphase) such as the interfacial transition zone around the aggregate or the finite thickness adhesive between the adherends. A problem in such cases is that the thickness of the interphase is about orders of magnitude less than the adjoining adherends. In such cases, if the crack propagation along the interphase is to be studied in detail, conventional finite elements which only offer a limited library of elements can lead to inefficient discretization. Several emerging methods, including isogeometric-meshfree methods [55], peridynamics [1], and nonlocal operator methods [73, 72, 71], provide mesh-free approaches for modeling fracture in composite materials.

The Virtual Element Method (VEM) [99, 101, 100, 18] provides a powerful and innovative alternative capable of addressing the issues of mesh-based approaches of solving partial differential equations. Unlike traditional finite element meshes that require significant efforts to maintain element shape quality and compatibility constraints, VEM can easily manage highly irregular geometries, non-conforming meshes, and hanging nodes [85] without compromising approximation accuracy or computational efficiency. Moreover, VEM is robust against mesh distortion, ensuring convergent results even on significantly distorted

elements. Furthermore, VEM can be easily integrated with FEM [86, 62]. Thus, VEM can be used in those parts of the domain which cannot be easily meshed with FEM, such as the interface between the matrix or inclusion. This can greatly simplify the numerical handling of mismatched meshes between different phases. This ease in mesh generation and conformity significantly reduces computational costs and pre-processing complexities that commonly arise in FEM-based approaches. Moreover, VEM's flexibility and accuracy on polygonal elements make it highly suitable for adaptive mesh refinement strategies [46, 107], which can further improve the efficiency of phase-field fracture simulations when applied to composite structures. Another alternative to VEM is the Polygonal Finite Element Method (PFEM) [90, 92] and its variants such as the Smoothed Finite Element Method (SFEM) [58]. These methods support polygonal elements, which can be employed for modeling composite fracture [45]. However, unlike VEM, PFEM requires the construction of Wachspress shape functions which would in turn require non-trivial numerical integration schemes.

Applications of VEM in the analysis of composite structures include statistical and computational homogenization of heterogeneous structures [80, 10, 59, 17, 61, 10], multiscale analysis of heterogeneous media [87, 82], realistic representation of concrete microstructure [50], meso-scale modeling of solid propellant [49], amongst others. However, limited studies have been done that focus on the modeling of interfacial failure and matrix cracking of composite materials within the VEM framework. In [88] the hard inclusion in a matrix was modeled by a single virtual element with multiple nodes, but only linear elastic analysis was performed and no debonding studies were carried out. In [37], the polycrystals were modeled as a single virtual element with multiple nodes and inter-granular fracture was simulated using CZM. These models demonstrated the versatility with which VEM can be used to model polycrystals or inclusions, but these models didn't consider the effect of matrix cracking, the kinking of an interfacial crack or the possibility of multiple crack nucleation which are some of the important failure modes in composite structures. In [12], interfacial elements were used between virtual elements to simulate matrix and interfacial failure, but it is well known that the use of interfacial elements can lead to mesh-sensitive results. Thus, there is a need to develop a robust framework which can efficiently capture matrix cracking, interfacial cracking and their interaction in composite structures in a VEM framework. This work aims to bridge these gaps. The key contributions of this work are:

- Development of a VEM framework that combines phase-field approach and cohesive zone fracture model for modeling fracture in composites.
- Demonstration of the robustness of proposed framework through quantitative validation against experimental results, specifically in challenging scenarios such as in meshes containing elements with hanging nodes or containing single polygonal elements over 100 edges.
- Numerical simulation for a range of damage mechanisms in composites, such as interfacial cracking, crack kinking from an interface, crack penetration or deflection across an interface, and multiple crack initiation, using the proposed framework.

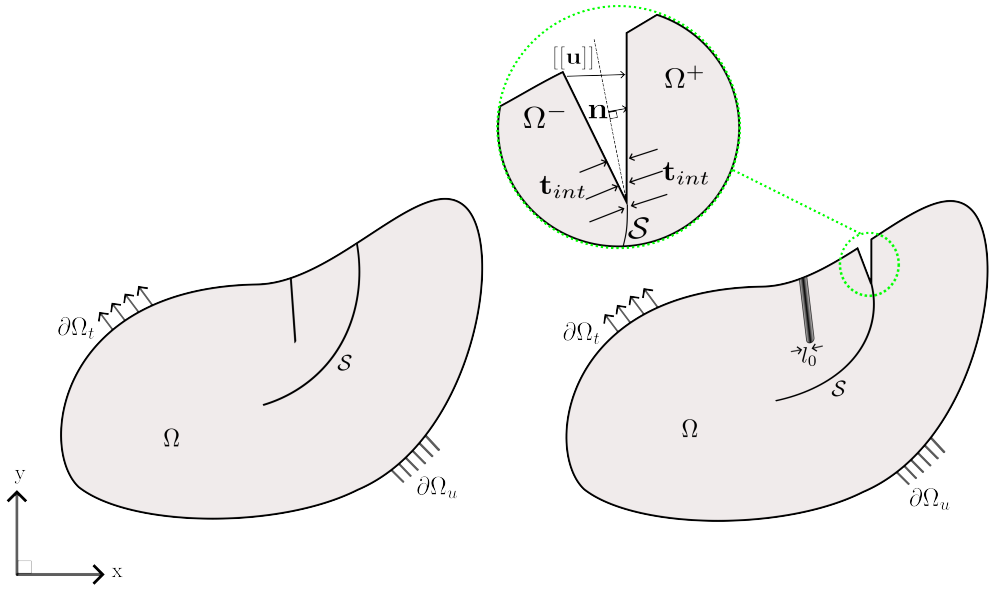

Figure 1: The body Ω along with the cohesive interface $\mathcal{S}$

- Extension of the framework through a coupled VEM–FEM formulation to simulate multiple crack nucleation in composites undergoing finite deformations.

Although the numerical investigations presented in this work are restricted to two-dimensional settings (plane stress and plane strain), the proposed VEM-based framework is not inherently limited to two dimensions. The present focus on 2D problems is motivated by the need for a systematic and transparent investigation of the efficiency of virtual elements in capturing the key damage mechanisms in composite materials, such as interfacial cracking, matrix cracking, and their mutual interaction, which can be most clearly analyzed in reduced-dimensional settings.

From a methodological standpoint, the proposed framework can be extended to three-dimensional composite fracture problems with suitable modifications to the projection spaces [91]. The inherent flexibility of polyhedral element shapes offered by the VEM in three dimensions further enables fracture simulations in complex structures, including 3D-printed lattices [110] and bolted composite assemblies [81, 20]. The ability of the virtual elements to discretize complex shaped geometries can be further employed for an efficient forward design of auxetic metamaterials [19].

The remainder of this manuscript is organized as follows. Section 2 derives the governing equations used to simulate failure in composite structures using the phase-field and cohesive-zone fracture models. The corresponding VEM discretization of these equations is presented in Section 3. Section 4 discusses the numerical simulations and their validation against experimental results from the literature, covering several representative damage mechanisms in composite structures. Finally, Section 5 concludes the study with a summary of the major findings.

2. Governing equations for damage in composite structures

2.1. Kinematics

Consider a solid body in the reference configuration, $\Omega \subset \mathbb{R}^{\delta}$ with dimension $\delta \in [2,3]$ and $\partial\Omega \subset \mathbb{R}^{\delta-1}$ be its boundary. Let, $\Omega^{+} \bigcup \Omega^{-} = \Omega$ and $\Omega^{+} \bigcap \Omega^{-} = \mathcal{S}$, where $\mathcal{S}$ represents an interface, as shown in Fig. 1. We describe the deformation of the body using the displacement field $\mathbf{u}$ along with the evolution of the ,field variable ϕ and the separation of the two opposing faces of the interface $\mathcal{S}$. Thus, for a material point $\mathbf{X} \in \Omega$ and time $t \in \mathcal{T} \subset \mathbb{R}$, the displacement field $\mathbf{u}(\mathbf{X},t)$, crack phase-field $\phi(\mathbf{X},t)$ and the displacement jump vector $[[\mathbf{u}]]$ are described as:

$$\mathbf{u} : \begin{cases} \Omega \times \mathcal{T} \rightarrow \mathbb{R}^{\delta}, \\ (\mathbf{X},t) \ \mapsto \mathbf{u}(\mathbf{X},t), \end{cases} \tag{1a}$$

$$\phi : \begin{cases} \Omega \times \mathcal{T} \rightarrow [0,1], \\ (\mathbf{X},t) \ \mapsto \phi(\mathbf{X},t). \end{cases} \tag{1b}$$

$$[[\mathbf{u}]] : \begin{cases} \Omega \times \mathcal{T} \rightarrow \mathbb{R}^{\delta}, \\ (\mathbf{X},t) \ \mapsto \mathbf{u}^{+}(\mathbf{X},t) - \mathbf{u}^{-}(\mathbf{X},t). \end{cases} \tag{1c}$$

The crack phase-field $\phi(\mathbf{X},t)$ is a smeared representation of the sharp crack geometry within the bulk of the body with $\phi(\mathbf{X},t) = 0$ representing a fully intact material while $\phi(\mathbf{X},t) = 1$ representing a fully damaged material. The displacement jump, $[[\mathbf{u}]]$, along the interface is a measure of crack propagation along the interface. $\mathbf{u}^{+}(\mathbf{X},t)$ and $\mathbf{u}^{-}(\mathbf{X},t)$ in Eq. (1c) denote the displacement vectors of the two opposing faces of the interface. Fig. 1 shows a 2D domain with the kinematic quantities. The crack phase field ϕ is a measure of the crack in the bulk of the body, while the displacement jump vector $[[\mathbf{u}]]$ is used to indicate the delamination along the interface. The infinitesimal strain tensor is used to describe the strains in the body and is given as:

$$\boldsymbol{\varepsilon} = \frac{1}{2}\left(\nabla\mathbf{u} + \nabla\mathbf{u}^{T}\right). \tag{2}$$

2.2. Macroscopic and microscopic balance laws using the principle of virtual power in the presence of a cohesive interface

The governing coupled equations of the damage evolution in the bulk and interface and the linear momentum balance can be derived by invoking the principle of virtual power [74, 69, 112]. Let $\dot{\mathbf{u}}$, $\nabla\dot{\mathbf{u}}$, $\dot{\phi}$, $\nabla\dot{\phi}$, $[[\dot{\mathbf{u}}]]$ be the kinematical descriptors. The macroscopic system is characterized by traction $\mathbf{t}(\mathbf{n})$, body force $\mathbf{b}$, which expends power over velocity $\dot{\mathbf{u}}$, and Cauchy stress tensor $\boldsymbol{\sigma}$, which expends power over displacement gradient rate $\nabla\dot{\mathbf{u}}$. The microscopic system in the bulk is characterized by the microscopic traction $\chi(\mathbf{n})$, scalar microscopic stress κ which expends power on the damage rate $\dot{\phi}$ and vector microscopic

stress $\boldsymbol{\zeta}$ which expend power over the damage gradient rate $\nabla\dot{\phi}$. Along the interface, the microscopic system is characterized by the microtraction $\mathbf{t}_{int}$ that expends power over the displacement jump vector rate, $[[\dot{\mathbf{u}}]]$. The internal and external virtual works $\mathcal{W}^{int}$ and $\mathcal{W}^{ext}$ respectively, for any part $\mathcal{P}$ of the body Ω and the part $\mathcal{S}_p$ of $\mathcal{S}$ intersecting $\mathcal{P}$ are given as:

$$W^{ext} = \int_{P\setminus S_p} \mathbf{b}\cdot\dot{\mathbf{u}}\, d\mathcal{P} \;+\; \int_{\partial\mathcal{P}} \left(\mathbf{t}(\mathbf{n})\cdot\dot{\mathbf{u}} + \chi(\mathbf{n})\cdot\dot{\phi}\right) d(\partial\mathcal{P}) \tag{3a}$$

$$W^{int} = \int_{P\setminus S_p} \left(\boldsymbol{\sigma} : \nabla\dot{\mathbf{u}} + \boldsymbol{\zeta}\cdot\nabla\dot{\phi} + \kappa\dot{\phi}\right) dP + \int_{S_p} \mathbf{t}_{int}\cdot[[\dot{\mathbf{u}}]] dS_p \tag{3b}$$

Let the set $\mathcal{V} = \left(\tilde{u}, \tilde{\phi}\right)$ consist of the virtual displacement and damage fields. The principle of virtual power can thus be expressed as:

$$\begin{aligned} &\int_{\partial\mathcal{P}} \left(\mathbf{t}(\mathbf{n})\cdot\tilde{u} + \chi(\mathbf{n})\cdot\tilde{\phi}\right) d(\partial\mathcal{P}) + \int_{P\setminus S_p} \mathbf{b}\cdot\tilde{u}\, d\mathcal{P} \;= \\ &\int_{P\setminus S_p} \left(\boldsymbol{\sigma} : \nabla\tilde{u} + \boldsymbol{\zeta}\cdot\nabla\tilde{\phi} + \kappa\tilde{\phi}\right) d\mathcal{P} \;+\; \int_{S_p} \mathbf{t}_{int}\cdot[[\dot{\tilde{\mathbf{u}}}]] dS_p. \end{aligned} \tag{4}$$

Motivated by the variational approach to fracture [15, 34], the free energy density function $\hat{\psi}$ is additively decomposed into two contributions, namely $\hat{\psi}^m$ and $\hat{\psi}^{int}$. The term $\hat{\psi}^m$ represents the free energy associated with deformation and damage mechanisms in the composite matrix, while $\hat{\psi}^{int}$ governs the delamination processes along material interfaces. A similar energetic decomposition has been adopted in several previous studies on coupled phase-field and cohesive-zone formulations for composites [75, 114, 95]. Since matrix damage is described using a phase-field fracture approach, $\hat{\psi}^m$ depends on the phase-field variable (ϕ), its gradient ($\nabla\phi$), and the strain tensor ($\boldsymbol{\varepsilon}$). In contrast, interfacial delamination is characterized by the displacement jump vector ($[[\mathbf{u}]]$). Accordingly, the total free energy density $\hat{\psi}$ can be written as:

$$\begin{aligned} \hat{\psi}(\phi, \nabla\phi, \boldsymbol{\varepsilon}, [[\mathbf{u}]]) =& \hat{\psi}^m(\phi, \nabla\phi, \boldsymbol{\varepsilon}) + \hat{\psi}^{int}([[\mathbf{u}]]) \\ =& \underbrace{\mathfrak{g}(\phi)\hat{\psi}^{elas}_{+}(\boldsymbol{\varepsilon}) + \hat{\psi}^{elas}_{-}(\boldsymbol{\varepsilon}) + \hat{\psi}^{frac}(\phi, \nabla\phi)}_{\text{matrix}} + \underbrace{\hat{\psi}^{int}([[\mathbf{u}]])}_{\text{interface}}. \end{aligned} \tag{5}$$

The matrix contribution $\hat{\psi}^m$ is further decomposed into tensile elastic energy ($\hat{\psi}^{elas}_{+}$), compressive elastic energy ($\hat{\psi}^{elas}_{-}$), and the fracture surface energy ($\hat{\psi}^{frac}$). The split of elastic energy into tensile and compressive components is physically motivated by the asymmetric damage response observed in composite materials: tensile principal strains promote crack initiation and propagation in the matrix, whereas compressive strains generally do not contribute to damage evolution [8, 63]. To account for this behavior, the degradation function $\mathfrak{g}(\phi)$ is applied exclusively to the tensile elastic energy $\hat{\psi}^{elas}_{+}$. Several choices for the degradation function exist in the literature, including linear, quadratic, and cubic forms [51]. In the present work, a quadratic degradation function is adopted, given by $\mathfrak{g}(\phi) = (1-\phi)^2$.

Using the spectral decomposition of the strain tensor $\boldsymbol{\varepsilon} = \sum_{i=1}^{3} \varepsilon_i \mathbf{n}_i \otimes \mathbf{n}_i$, the tensile and compressive elastic energy densities can be expressed as: [63]

$$\hat{\psi}^{elas}(\boldsymbol{\varepsilon})_{\pm} = \frac{\lambda}{2}\langle \varepsilon_1 + \varepsilon_2 + \varepsilon_3 \rangle_{\pm} + \mu \left(\langle \varepsilon_1 \rangle_{\pm}^2 + \langle \varepsilon_2 \rangle_{\pm}^2 + \langle \varepsilon_3 \rangle_{\pm}^2 \right), \tag{6}$$

where λ and μ are the Lamé parameters, and $\langle \cdot \rangle_{\pm}$ denote the ramp functions defined as $\langle x \rangle_{+} = (|x| + x)/2$ and $\langle x \rangle_{-} = (|x| - x)/2$.

Since matrix cracking is represented in a smeared sense through the phase-field variable (ϕ), crack initiation and propagation are governed by the fracture surface free energy density $\hat{\psi}^{frac}$. In this work, $\hat{\psi}^{frac}$ is defined using the AT2 phase-field model [63], expressed in terms of the fracture toughness G_c and the regularization length l_0 as:

$$\hat{\psi}^{frac} = \frac{G_c}{2l_0} \left(\phi^2 + l_0^2 \nabla\phi \cdot \nabla\phi \right). \tag{7}$$

The interface energy density $\hat{\psi}^{int}([[\mathbf{u}]])$ governs energy dissipation along material interfaces. For interfacial cracks, the local stress state at the crack tip is generally of mixed-mode nature, even when the externally applied loading is nominally Mode I [47]. Such mixed-mode conditions commonly arise due to elastic modulus or fracture toughness mismatch between adjoining phases in composite materials, for example between the matrix and fibers or between adjacent plies in layered composites. To capture mixed-mode interfacial crack propagation, several potential-based and non-potential-based cohesive zone models have been proposed in the literature [77]. Potential-based cohesive zone models may be broadly classified into polynomial-based formulations [67, 35, 79] and exponential-based formulations [68, 109, 14]. In the present work, we adopt the potential-based cohesive zone model proposed by Park et al. [79], and the corresponding interface free energy density is defined as follows:

$$\begin{aligned} \hat{\psi}^{int}([[\mathbf{u}]]) = & min(G_{int}^n, G_{int}^t) + \\ & \left(\Gamma_n \left(1 - \frac{[[\mathbf{u}]] \cdot \mathbf{n}}{\delta_n} \right)^{\alpha} \left(\frac{m}{\alpha} + \frac{[[\mathbf{u}]] \cdot \mathbf{n}}{\delta_n} \right)^{m} + \langle G_{int}^n - G_{int}^t \rangle \right) \times \\ & \left(\Gamma_t \left(1 - \frac{|[[\mathbf{u}]]| \cdot \mathbf{t}}{\delta_t} \right)^{\beta} \left(\frac{n}{\beta} + \frac{|[[\mathbf{u}]]| \cdot \mathbf{t}}{\delta_t} \right)^{n} + \langle G_{int}^t - G_{int}^n \rangle \right) \end{aligned} \tag{8}$$

where Γ_n, Γ_t, δ_n, δ_t, G_{int}^n, G_{int}^t, α, β are material constants. $[[\mathbf{u}]] \cdot \mathbf{n}$, $[[\mathbf{u}]] \cdot \mathbf{t}$ represent the normal and tangential components of $[[\mathbf{u}]]$. Taking arbitrary values of the virtual fields $\mathcal{V}$, in Eq.(4), using the first and second laws of thermodynamics, the free energy density function in Eq.(5) and incorporating crack irreversibility through a history function [63] ($\mathscr{H}$), the macroforce and microforce balance laws and the associated boundary conditions

can be expressed as [36, 24]:

$$\nabla \cdot \boldsymbol{\sigma} + \mathbf{b} = \mathbf{0} \quad \text{in} \quad \Omega \setminus S, \tag{9a}$$

$$\boldsymbol{\sigma} \cdot \mathbf{n} = \bar{\mathbf{t}} \quad \text{on} \quad \partial\Omega_t, \tag{9b}$$

$$\mathbf{u} = \bar{\mathbf{u}} \quad \text{on} \quad \partial\Omega_u, \tag{9c}$$

$$\boldsymbol{\sigma}|_S \mathbf{n} = \mathbf{t}_{int} \quad \text{on} \quad S, \tag{9d}$$

$$[[\boldsymbol{\sigma}\mathbf{n}]] = {\mathbf{t}_{int}}^{+} - {\mathbf{t}_{int}}^{-} = \mathbf{0} \quad \text{on} \quad S. \tag{9e}$$

$$\frac{G_c}{l_0}\left(\phi - l_0^2 \Delta\phi\right) = 2\left(1-\phi\right)\mathscr{H} \quad \text{in} \quad \Omega, \tag{9f}$$

$$\nabla\phi \cdot \mathbf{n} = 0 \quad \text{on} \quad \partial\Omega, \tag{9g}$$

where the Cauchy stress tensor ($\boldsymbol{\sigma}$), traction on the interface S, and the history function ($\boldsymbol{\sigma}$) are defined as:

$$\boldsymbol{\sigma} = (1-\phi)^2 \frac{\partial \hat{\psi}_+^{elas}(\boldsymbol{\varepsilon})}{\partial \boldsymbol{\varepsilon}} + \frac{\partial \hat{\psi}_-^{elas}(\boldsymbol{\varepsilon})}{\partial \boldsymbol{\varepsilon}} \quad \text{in} \quad \Omega \setminus S, \tag{10a}$$

$$\boldsymbol{\sigma}|_S \mathbf{n} = \mathbf{t}_{int} = \frac{\partial \hat{\psi}^{int}([[\mathbf{u}]])}{\partial [[\mathbf{u}]]} \quad \text{on} \quad S, \tag{10b}$$

$$\mathscr{H}(\hat{\psi}_+^{elas}(\boldsymbol{\varepsilon})) = \max_{s\in[0,\tau]} \hat{\psi}_+^{elas}(\boldsymbol{\varepsilon}(s)) \quad \text{in} \quad \Omega. \tag{10c}$$

3. Discretization of the governing equation

3.1. Mathematical Preliminaries

We consider a 2D domain shown in Fig. 1 which is discretized by the set $\mathcal{E}_h^V \cup \mathcal{E}_h^C$, where $\mathcal{E}_h^V$ denotes the discretization of the domain $\Omega \setminus S$, and $\mathcal{E}_h^C$ denotes the discretization of the domain S. $\mathcal{E}_h^V$ consists of 2D virtual elements consisting of convex or non-convex polygons. In contrast, $\mathcal{E}_h^C$ consists of elements formed by duplicating the nodes of $\mathcal{E}_h^V$ common to S. An element of $\mathcal{E}_h^C$ is called the cohesive element, has four nodes, and is formed by each consecutive pair of duplicate nodes. Fig. 2a shows a discretized region containing the interface. The four-noded cohesive elements (E_c) are formed by duplicating the consecutive nodes of the adjoining 9-noded virtual elements (E_v). We show the nominal thickness of a cohesive element only for representation purposes.

3.1.1. Virtual element

Fig. 2b, shows a 9-noded virtual element, with vertices V_1 to V_9 and edges e_1 to e_9. n_{e_8} denotes the outward normal corresponding to edge e_8. A 9-noded element is possible since VEM allows the use of any arbitrary number of vertices. Similarly, for a virtual element with a total number of vertices as N_v, the edges can be denoted as $e_1, e_2, \ldots e_{N_v}$ and the vertices can be denoted as $V_1, V_2, \ldots, V_{N_v}$. e_i denotes the edge between the vertices V_i and V_{i+1}. Since $V_{N_v} \equiv V_1$, e_{N_v} denotes the edge between the vertices V_{N_v} and V_1.

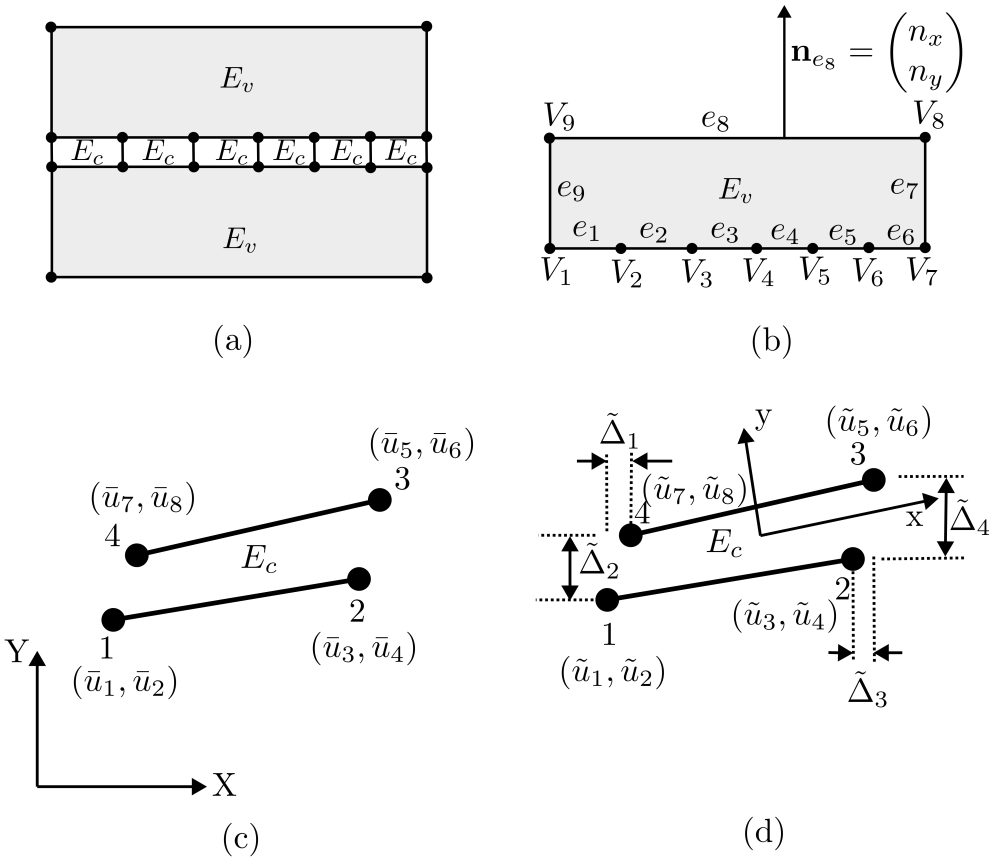

Figure 2: Discretization of the domain (a) Virtual elements (E_v) with cohesive elements (E_c) along the interface (b) A 9-noded virtual element (E_v) (c) A cohesive element (E_c) in global coordinates (d) A cohesive element (E_c) in local coordinates

Let $\mathrm{P}_k(E)$ denote the space of complete polynomials of degree k defined over the element E_v. A convenient choice of basis for $\mathrm{P}_k(E)$ is the set $\mathrm{M}_k(E)$, which is composed of scaled monomials of total degree less than or equal to k. In two dimensions, for the case $k = 1$ with a single degree of freedom per node, the basis set $\mathrm{M}_1(E)$ takes the form:

$$\mathrm{M}_1(E) = \{m_1, m_2, m_3\} = \big\{1, \xi, \eta\big\}, \tag{11}$$

where the scaled monomials ξ and η are defined as:

$$\xi = \frac{x - x_c}{h_E}, \tag{12a}$$

$$\eta = \frac{y - y_c}{h_E}. \tag{12b}$$

For the case of two-dimensional elastostatics with $k = 1$, each node possesses two degrees of freedom. Consequently, the vector-valued polynomial space is defined as $\mathbf{M}_1(E) \equiv [\mathrm{M}_1(E)]^2$, which has dimension 6. The corresponding basis can be expressed as:

$$\begin{aligned}\mathbf{M}_1(E) = \{\mathbf{m}_1, \mathbf{m}_2, \mathbf{m}_3, \mathbf{m}_4, \mathbf{m}_5, \mathbf{m}_6\} = \\ \left[\begin{pmatrix}1\\0\end{pmatrix}, \begin{pmatrix}0\\1\end{pmatrix}, \begin{pmatrix}-\eta\\ \xi\end{pmatrix}, \begin{pmatrix}\eta\\ \xi\end{pmatrix}, \begin{pmatrix}\xi\\0\end{pmatrix}, \begin{pmatrix}0\\ \eta\end{pmatrix}\right],\end{aligned} \tag{13}$$

where the first three vectors, $\mathbf{m}_1, \mathbf{m}_2, \mathbf{m}_3$, are chosen to ensure that rigid body motions are represented.

These preliminaries form the foundation for the derivation of the elemental stiffness matrix for general polygonal elements using VEM, which will be employed in the discretisation of the governing equations of damage evolution and equilibrium in subsequent sections.

3.1.2. Cohesive element

Fig. 2c and Fig. 2d show the displacement at the nodes of the cohesive element in terms of global and local coordinates, respectively. The stiffness matrix of a cohesive element is written in terms of the local separation vector ($\boldsymbol{\Delta} = \begin{Bmatrix}\Delta_t & \Delta_n\end{Bmatrix}^T$), which can be expressed in terms of the global displacement quantities ($\{\bar{\mathbf{U}}\} = \begin{Bmatrix}\bar{u}_1 & \bar{u}_2 & \cdots & \bar{u}_8\end{Bmatrix}^T$) as [78]:

$$\{\boldsymbol{\Delta}\} = [B^c]\{\bar{\mathbf{U}}\}, \tag{14}$$

where, $[B^c] = [N^c][L^c][R^c]$. $[N^c]$ consists of the linear shape functions of the cohesive element, $[L^c]$ relates the local displacement quantities ($\{\tilde{\mathbf{U}}\} = \begin{Bmatrix}\tilde{u}_1 & \tilde{u}_2 & \cdots & \tilde{u}_8\end{Bmatrix}^T$) to the nodal local separation variables ($\{\tilde{\boldsymbol{\Delta}}\} = \begin{Bmatrix}\tilde{\Delta}_1 & \tilde{\Delta}_2 & \tilde{\Delta}_3 & \tilde{\Delta}_4\end{Bmatrix}^T$) and $[R^c]$ is the rotation matrix which is

used to relate the local and global displacement quantities. These can be expressed as:

$$[N^c] = \begin{bmatrix} \frac{1-t}{2} & 0 & \frac{1+t}{2} & 0 \\ 0 & \frac{1-t}{2} & 0 & \frac{1+t}{2} \end{bmatrix}, \tag{15a}$$

$$[L^c] = \begin{bmatrix} -1 & 0 & 0 & 0 & 0 & 0 & 1 & 0 \\ 0 & -1 & 0 & 0 & 0 & 0 & 0 & 1 \\ 0 & 0 & -1 & 0 & 1 & 0 & 0 & 0 \\ 0 & 0 & 0 & -1 & 0 & 1 & 0 & 0 \end{bmatrix}, \tag{15b}$$

$$[R^c] = \begin{bmatrix} \mathbf{\Theta} & \mathbf{0} & \mathbf{0} & \mathbf{0} \\ \mathbf{0} & \mathbf{\Theta} & \mathbf{0} & \mathbf{0} \\ \mathbf{0} & \mathbf{0} & \mathbf{\Theta} & \mathbf{0} \\ \mathbf{0} & \mathbf{0} & \mathbf{0} & \mathbf{\Theta} \end{bmatrix}. \tag{15c}$$

Where $0 \leq t \leq 1$ is a parameter in Eq.(15a), $\mathbf{0}$ is a square matrix of size 2 in Eq.(15c) and $\mathbf{\Theta}$ is a 2×2 matrix given by,

$$\mathbf{\Theta} = \begin{bmatrix} cos\theta & sin\theta \\ -sin\theta & cos\theta \end{bmatrix}, \tag{16}$$

where, θ is the angle between the global and local coordinate systems.

3.2. Virtual element spaces

The weak form of the governing equations describing the matrix failure using the phase field fracture model and the interfacial failure using the cohesive zone model can be stated as:

$$\begin{cases} \text{Find } \phi \in \mathcal{V}_\phi = H_0^1(\Omega) \text{ and } \mathbf{u} \in \mathcal{V}_\mathbf{u} = [H_0^1(\Omega)]^2 \text{ such that:} \\ \mathcal{B}_\phi(\phi, v_\phi) = L_\phi(v_\phi), \quad \forall v_\phi \in \mathcal{V}_\phi, \\ \mathcal{B}_\mathbf{u}^C(\mathbf{u}, \mathbf{v_u}) = L_\mathbf{u}(\mathbf{v_u}), \quad \forall \mathbf{v_u} \in \mathcal{V}_\mathbf{u}, \end{cases} \tag{17}$$

where, $H_0^1(\Omega)$ indicates the first-order Sobolev space. The bilinear forms $\mathcal{B}_\phi^m(\phi, v_\phi)$, $\mathcal{B}_\mathbf{u}^C(\mathbf{u}, \mathbf{v_u})$ and the linear form $L_\phi^m(v_\phi)$, $L_\mathbf{u}^C(\mathbf{v_u})$ are given as:

$$\mathcal{B}_\phi^m(\phi, v_\phi) = \underbrace{\int_{\Omega \setminus S} (G_c l_0) \nabla\phi \cdot \nabla v_\phi \, d\Omega + \int_{\Omega \setminus S} \left(\frac{G_c}{l_0} + 2\mathscr{H} \right) \phi v_\phi \, d\Omega}_{\text{matrix}}, \tag{18a}$$

$$\mathcal{B}_\mathbf{u}^C(\mathbf{u}, \mathbf{v_u}) = \underbrace{\int_{\Omega \setminus S} \boldsymbol{\sigma}(\mathbf{u}) : \boldsymbol{\epsilon}(\mathbf{v_u}) \, d\Omega}_{\text{matrix}} + \underbrace{\int_S \mathbf{t}_{int}([[\mathbf{u}]]) \cdot [[\mathbf{v_u}]] dS}_{\text{interface}}, \tag{18b}$$

$$L_\phi^m(v_\phi) = \underbrace{\int_{\Omega \setminus S} 2\mathscr{H} v_\phi \, d\Omega}_{\text{matrix}}, \tag{18c}$$

$$L_\mathbf{u}^C(\mathbf{v_u}) = \underbrace{\int_{\partial\Omega} \mathbf{v_u} \cdot \bar{\mathbf{t}} \, d(\partial\Omega_t)}_{\text{matrix}}. \tag{18d}$$

Eq.(18) highlights the bilinear forms associated with the matrix and interface domain. It can be observed that the bilinear form of the displacement subproblem has an additional contribution due to the cohesive separation along the interfaces. The bilinear form $\mathcal{B}_{\phi}^{m}(\phi, v_{\phi})$ corresponds to the phase field fracture modeling in the matrix. In contrast, the bilinear form $\mathcal{B}_{\mathbf{u}}^{C}(\mathbf{u}, \mathbf{v_u})$ describes the deformation of the body, Ω, which includes the separation along the pre-defined interface S.

Let $\mathcal{V}_{\phi,h}$ and $\mathcal{V}_{\mathbf{u},h}$ denote the finite dimensional subspaces of $\mathcal{V}_{\phi}$ and $\mathcal{V}_{\mathbf{u}}$ repectively. These spaces are constructed by the assembly of $\mathcal{V}_{\phi,h}(E)$ and $\mathcal{V}_{\mathbf{u},h}(E)$ over the elements $E \in \mathcal{E}_h^V \cup \mathcal{E}_h^C$. The local virtual element spaces, $\mathcal{V}_{\phi,h}(E)$ and $\mathcal{V}_{\mathbf{u},h}(E)$ over an element E, are defined as:

$$\begin{aligned}\mathcal{V}_{\phi,h}(E) \coloneqq \big\{ & v_{\phi,h} : v_{\phi,h} \in H^1(E), \quad \Delta v_{\phi,h} = 0, \quad v_{\phi,h}|_e \in \mathrm{P}_1(e), \\ & \forall e \in \partial E, \quad v_{\phi,h}|_{\partial E} \in C^0(\partial E) \big\}, \end{aligned} \tag{19a}$$

$$\begin{aligned}\mathcal{V}_{\mathbf{u},h}(E) \coloneqq \big\{ & \mathbf{v}_{\mathbf{u},h} : \mathbf{v}_{\mathbf{u},h} \in [H^1(E)]^2, \quad \Delta \mathbf{v}_{\mathbf{u},h} \in [\mathrm{P}_1(e)]^2, \\ & \mathbf{v}_{\mathbf{u},h}|_e \in [\mathrm{P}_1(e)]^2 \quad \forall e \in \partial E, \quad \mathbf{v}_{\mathbf{u},h}|_{\partial E} \in C^0(\partial E) \big\}. \end{aligned} \tag{19b}$$

For $\mathcal{V}_{\phi,h}(E)$ and $\mathcal{V}_{\mathbf{u},h}(E)$ defined as in Eq. (19), the degrees of freedom can be chosen as the values of ϕ_h and $\mathbf{u}_h(u_h^x, u_h^y)$ at the vertices of E. Thus the dimension of $\mathcal{V}_{\phi,h}(E)$ and $\mathcal{V}_{\mathbf{u},h}(E)$ is N_v and $2N_v$ respectively. The global virtual element space $\mathcal{V}_{\phi,h}$ and $\mathcal{V}_{\mathbf{u},h}$ can now be defined as:

$$\mathcal{V}_{\phi,h} \coloneqq \big\{ v_{\phi,h} : v_{\phi,h} \in H_0^1(\Omega), \quad v_{\phi,h}|_e \in \mathcal{V}_{\phi,h}(E) \quad \forall E \in \mathcal{E}_h \big\}, \tag{20a}$$

$$\mathcal{V}_{\mathbf{u},h} \coloneqq \big\{ \mathbf{v}_{\mathbf{u},h} : \mathbf{v}_{\mathbf{u},h} \in [H_0^1(\Omega)]^2, \quad \mathbf{v}_{\mathbf{u},h}|_e \in \mathcal{V}_{\mathbf{u},h}(E) \quad \forall E \in \mathcal{E}_h \big\}. \tag{20b}$$

3.3. Element stiffness matrices

The element stiffness matrix for the damage ($\mathbf{K}_{\phi,E}^c$) and displacement subproblem ($\mathbf{K}_{\mathbf{u},E}^c$), corresponding to the bilinear forms given by Eq.(18a) and Eq.(18b) can be expressed as:

$$\mathbf{K}_{\phi,E}^c = \mathbf{K}_{\phi,E}\,, \tag{21a}$$

$$\mathbf{K}_{\mathbf{u},E}^c = \mathbf{K}_{\mathbf{u},E} + \mathbf{K}_{TSL}, \tag{21b}$$

where $\mathbf{K}_{\phi,E}$ and $\mathbf{K}_{\mathbf{u},E}$ represent the stiffness matrix corresponding to the bilinear form of the matrix domain, as shown in Eq.(18a) and Eq.(18b) respectively. $\mathbf{K}_{TSL}$ represents the stiffness matrix corresponding to the bilinear form of the interface domain, as shown in Eq.(18b). The following subsections give the explicit form of these stiffness matrices.

3.3.1. Elemental stiffness matrix for the matrix domain

Since the matrix domain of the composite is discretized using the virtual elements, the stiffness matrices, $\mathbf{K}_{\phi,E}$ and $\mathbf{K}_{\mathbf{u},E}$ can be computed by using the projection operators and the orthogonality conditions [100]. We assume the projection operators Π_{ϕ}^{∇}, and $\Pi_{\mathbf{u},m}^{\nabla}$ project the restriction onto each element of the finite dimensional bilinear forms $\mathcal{B}_{\phi}^{m}(\phi, v_{\phi})$ and the matrix component of the bilinear form $\mathcal{B}_{\mathbf{u}}^{C}(\mathbf{u}, \mathbf{v_u})$ to the polynomial spaces $\mathrm{M}_1(E)$ and $\mathbf{M}_1(E)$ respectively. These projection operators can be expressed as [85]:

$$\Pi_{\phi}^{\nabla} = G^{-1}B, \tag{22a}$$

$$\Pi_{\mathbf{u},m}^{\nabla} = \mathbf{G}^{-1}\mathbf{B}, \tag{22b}$$

where the matrices G, B, $\mathbf{G}$ and $\mathbf{B}$ can be expressed as:

$$G_{\alpha\beta} = \begin{cases} \dfrac{1}{N_v}\displaystyle\sum_{j=1}^{N_v} m_\beta(V_j) & (\alpha = 1 \quad \& \quad \beta = 1,2,3), \\ \displaystyle\int_E \nabla m_\alpha \cdot \nabla m_\beta \, dE & (\text{otherwise}), \end{cases} \tag{23a}$$

$$B_{\alpha i} = \begin{cases} \dfrac{1}{N_v}\displaystyle\sum_{j=1}^{N_v} \psi_i(V_j) & (\alpha = 1 \quad \& \quad i = 1,2,\cdots,N_v), \\ \displaystyle\int_E \nabla m_\alpha \cdot \nabla \psi_i \, dE & (\text{otherwise}). \end{cases} \tag{23b}$$

$$\mathbf{G}_{\bar{\alpha}\bar{\beta}} = \begin{cases} \dfrac{1}{N_v}\displaystyle\sum_{j=1}^{N_v} \mathbf{m}_{\bar{\alpha}}(\mathbf{x}_j).\mathbf{m}_{\bar{\beta}}(\mathbf{x}_j) & (\bar{\alpha} = 1,2,3), \\ \displaystyle\sum_{j=1}^{N_v} \mathbf{m}_{\bar{\beta}}(\mathbf{x}_j) \cdot \boldsymbol{\sigma}(\mathbf{m}_{\bar{\alpha}}) \left(\frac{|e_{j-1}|}{2}\mathbf{n}_{e_{j-1}} + \frac{|e_j|}{2}\mathbf{n}_{e_j} \right) & (\text{otherwise}), \end{cases} \tag{23c}$$

$$\mathbf{B}_{\bar{\alpha}\mathtt{i}} = \begin{cases} \dfrac{1}{N_v}\displaystyle\sum_{j=1}^{N_v} \mathbf{m}_{\bar{\alpha}}(\mathbf{x}_j).\boldsymbol{\Psi}_{\mathtt{i}}(\mathbf{x}_j) & (\bar{\alpha} = 1,2,3), \\ \displaystyle\sum_{j=1}^{N_v} \boldsymbol{\Psi}_{\mathtt{i}}(\mathbf{x}_j) \cdot \boldsymbol{\sigma}(\mathbf{m}_{\bar{\alpha}}) \left(\frac{|e_{j-1}|}{2}\mathbf{n}_{e_{j-1}} + \frac{|e_j|}{2}\mathbf{n}_{e_j} \right) & (\text{otherwise}). \end{cases} \tag{23d}$$

In Eq.(23b) and Eq.(23d), ψ_i and $\boldsymbol{\Psi}_{\mathtt{i}}$ denote the N_v and $2N_v$ canonical basis functions of the spaces $\mathcal{V}_{\phi,h}(E)$ and $\mathcal{V}_{\mathbf{u},h}(E)$, respectively. In particular, $\psi_i(V_j) = \delta_{ij}$, where δ_{ij} is the Kronecker delta symbol and $i,j = 1,2,\cdots,N_v$, $\boldsymbol{\Psi}_i = \{\psi_i \ 0\}^T$ and $\boldsymbol{\Psi}_{N^v+i} = \{0 \ \psi_i\}^T$. The Cauchy stress tensor is coupled to the phase field nodal-average phase field and is computed as:

$$\boldsymbol{\sigma}(\mathbf{m}_{\bar{\alpha}}) = (1-\bar{\phi})^2 \mathbf{C}_0 \boldsymbol{\epsilon}(\mathbf{m}_{\bar{\alpha}}), \tag{24}$$

where, $\mathbf{C}_0$ is the undamaged elasticity constitutive matrix, and $\bar{\phi}$ is the nodal average phase field defined as:

$$\bar{\phi} = \sum_{j=1}^{N_v} \frac{\phi_j}{N_v}. \tag{25}$$

The stiffness matrix, $\mathbf{K}_{\phi,E}$ and $\mathbf{K}_{\mathbf{u},E}$ can thus be expressed as:

$$\mathbf{K}_{\phi,E} = \underbrace{(\Pi_\phi^\nabla)^T \left((G_c l_0)\bar{G} + \left(\frac{G_c}{l_0} + 2\mathscr{H} \right) H \right) (\Pi_\phi^\nabla)}_{\text{Consistency term}} + \underbrace{(G_c l_0)(\mathbf{I} - D\Pi_\phi^\nabla)^T(\mathbf{I} - D\Pi_\phi^\nabla)}_{\text{Stability term}}, \tag{26a}$$

$$\mathbf{K}_{\mathbf{u},E} = \underbrace{(\Pi_{\mathbf{u},m}^\nabla)^T \bar{\mathbf{G}} (\Pi_{\mathbf{u},m}^\nabla)}_{\text{Consistency term}} + \underbrace{(\mathbf{I} - \mathbf{D}\Pi_{\mathbf{u},m}^\nabla)^T \mathbf{S}_E^d (\mathbf{I} - \mathbf{D}\Pi_{\mathbf{u},m}^\nabla)}_{\text{Stability term}}, \tag{26b}$$

where the matrices $\bar{G}$ and $\bar{\mathbf{G}}$ are the G and $\mathbf{G}$ matrices in Eq.(23a) and Eq.(23c) with the first row and the first three rows set to zero, respectively. The matrix H is given by:

$$H = \int_E m_\alpha m_\beta \, dE. \tag{27}$$

The matrices D and $\mathbf{D}$ in Eq.(26) are used to represent the projection operators in canonical bases and are defined as:

$$D_{i\alpha} = \mathtt{dof}_i(m_\alpha), \tag{28a}$$
$$\mathbf{D}_{\mathtt{i}\bar{\alpha}} = \mathtt{dof}_{\mathtt{i}}(\mathbf{m}_{\bar{\alpha}}), \tag{28b}$$

where, the $\mathtt{dof}_k(\cdot)$ operator gives the value of any input at the k^{th} degree of freedom. The history energy function ($\mathscr{H}$) in Eq.(26) is computed using the volume average strain measure, which can be computed as:

$$\boldsymbol{\varepsilon}_{avg}(E) = \frac{1}{V}\int_V \boldsymbol{\varepsilon}\, dE = \frac{\nabla\left(\boldsymbol{\Pi}^{\nabla}_{\mathbf{u},m}\mathbf{u}\right) + \nabla\left(\boldsymbol{\Pi}^{\nabla}_{\mathbf{u},m}\mathbf{u}^T\right)}{2V}, \tag{29}$$

where V is the volume of the virtual element E_v.

3.3.2. Elemental stiffness matrix for the interface domain

The elemental stiffness matrix for the cohesive element can be derived by linearising the bilinear form corresponding to the interface domain in Eq.(18b) and can be expressed as:

$$\mathbf{K}_{TSL} = \int_S [B^c]^T [D^c][B^c]\, dS, \tag{30}$$

where, the matrix $[D^c]$ can be derived using the PPR potential, $\hat{\psi}^{int}$ as:

$$[D^c] = \begin{bmatrix} D^c_{tt} & D^c_{tn} \\ D^c_{nt} & D^c_{nn} \end{bmatrix} = \begin{bmatrix} \frac{\partial^2\hat{\psi}^{int}}{\partial\Delta_t^2} & \frac{\partial^2\hat{\psi}^{int}}{\partial\Delta_t\partial\Delta_n} \\ \frac{\partial^2\hat{\psi}^{int}}{\partial\Delta_n\partial\Delta_t} & \frac{\partial^2\hat{\psi}^{int}}{\partial\Delta_n^2} \end{bmatrix}. \tag{31}$$

3.4. VEM-FEM hybrid discretization strategy

We now describe a framework for combining FEM and VEM discretizations within a unified displacement-based formulation. This approach is particularly useful in situations where virtual elements offer significant flexibility for discretizing complex geometries, or when a VEM formulation for a given governing equation is not yet available.

In this work, we adopt a hybrid VEM - FEM discretization framework for modeling fracture in hyperelastic composite materials containing inclusions, where the matrix undergoes finite deformation. We use four-noded linear finite elements (FE) to discretize the matrix regions, and first-order polygonal virtual elements (VE) with an arbitrary number of nodes to

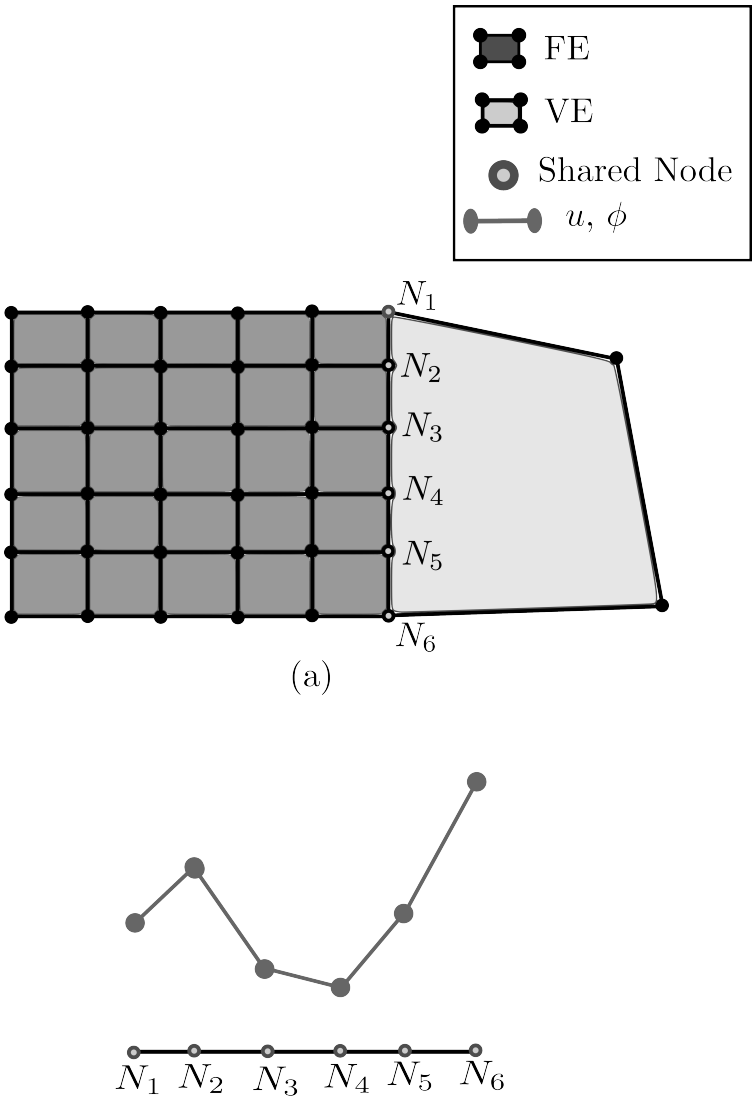

Figure 3: Schematic illustration of the hybrid VEM–FEM discretization strategy. (a) Standard four-noded linear finite elements are employed together with eight-noded polygonal virtual elements.(b) Linear variation of the displacement and phase-field degrees of freedom along the shared interface.

discretize the inclusion as a single polygonal element. The interface can be discretized using zero-thickness four-noded cohesive elements (CE). All these element types exhibit linear displacement variation along their element boundaries. As a result, displacement compatibility across VEM - FEM interfaces is naturally satisfied, and no additional coupling constraints or mortar formulations are required. The correctness of this hybrid discretization strategy can be verified through standard patch tests, as demonstrated in [62].

A schematic illustration of the hybrid VEM - FEM discretization and the associated displacement compatibility across the interfaces is shown in Fig. 3. Figure 3(a) shows four-noded linear finite elements sharing common edges with eight-noded linear virtual elements. Owing to the local virtual element spaces defined in Eq. 19, both the displacement $\mathbf{u}$ and the phase-field ϕ degrees of freedom vary linearly and remain continuous across element edges. Consequently, the finite and virtual elements are fully compatible along their shared interfaces. This compatibility is schematically illustrated in Fig. 3(b) for both the displacement and phase-field degrees of freedom. Note that the cohesive elements used are zero-thickness elements placed along the shared edges and are therefore not shown here for brevity.

3.4.1. Finite element stiffness matrices for phase-field fracture in hyperelastic matrix undergoing finite deformation

In the finite deformation setting, the deformation of the body is described by the deformation mapping $\boldsymbol{\varphi}(\mathbf{X})$, with the deformation gradient,

$$\mathbf{F} = \nabla_{\mathbf{X}} \boldsymbol{\varphi} = \mathbf{I} + \nabla_{\mathbf{X}} \mathbf{u}, \tag{32}$$

where, $\mathbf{X}$ denotes the material coordinates in the reference configuration and $\mathbf{I}$ is the Identity tensor. The phase-field variable $\phi \in [0, 1]$ retains the same physical interpretation as in Section 2, with $\phi = 0$ representing intact material and $\phi = 1$ denoting fully developed fracture.

The stored elastic energy density is defined per unit reference volume and expressed in terms of invariants of the deformation gradient. A compressible Neo-Hookean model is adopted,

$$\hat{\psi}^{\text{elas}}(\mathbf{F}) = \frac{\kappa}{2}(\log J)^2 + \frac{\mu}{2}(J^{\frac{-2}{3}} I_1 - 3), \tag{33}$$

where $J = \det \mathbf{F}$, $I_1 = \text{tr}(\mathbf{F}^T \mathbf{F})$, and κ and μ denote the bulk and shear moduli, respectively.

To ensure that fracture evolution is driven only by tensile deformation, the elastic energy density is decomposed into tensile and compressive contribution [83]. Specifically, the tensile part of the elastic energy is defined as:

$$\hat{\psi}_+^{\text{elas}}(I_1, J) = \begin{cases} \dfrac{\kappa}{2}(\log J)^2 + \dfrac{\mu}{2}(J^{\frac{-2}{3}} I_1 - 3), & J \geq 1, \\ \dfrac{\mu}{2}(J^{\frac{-2}{3}} I_1 - 3), & J < 1, \end{cases} \tag{34}$$

while the compressive contribution is obtained as:

$$\hat{\psi}_-^{\text{elas}}(I_1, J) = \hat{\psi}^{\text{elas}}(I_1, J) - \hat{\psi}_+^{\text{elas}}(I_1, J). \tag{35}$$

The total degraded elastic energy density is then written as:

$$\hat{\psi}^{\text{elas}}(\mathbf{F},\phi) = \hat{\psi}^{\text{elas}}_{-}(\mathbf{F}) + \left(\mathfrak{g}(\phi)+k\right)\hat{\psi}^{\text{elas}}_{+}(\mathbf{F}), \tag{36}$$

where $g(\phi) = (1-\phi)^2$ is the degradation function and $k \ll 1$ is a numerical stabilization parameter ensuring well-posedness of the governing equations. The first Piola - Kirchoff stress can be expressed as:

$$\mathbf{P}^I = (1-\phi)^2 \frac{\partial \hat{\psi}^{elas}_{+}(\mathbf{F})}{\partial \mathbf{F}} + \frac{\partial \hat{\psi}^{elas}_{-}(\mathbf{F})}{\partial \mathbf{F}} \tag{37}$$

In this work, the finite element discretization of the matrix domain, consists of four-noded linear quadrilateral elements. Thus ϕ_h and $\mathbf{u}_h$ can be expressed in terms of their nodal values $[\bar{\phi}]$ and $[\bar{\mathbf{u}}]$ as:

$$\phi_h = [\mathbf{N}_\phi][\bar{\phi}], \tag{38a}$$

$$\mathbf{u}_h = [\mathbf{N}_\mathbf{u}][\bar{\mathbf{u}}], \tag{38b}$$

where, $[\mathbf{N}_\phi]$, $[\mathbf{N}_\mathbf{u}]$, represent the known finite element shape function matrices of the damage and displacement field. The gradient of these quantities can be expressed using the known matrices $[\mathbf{B}_\phi]$ and $[\mathbf{B}_\mathbf{u}]$, respectively. The fracture energy functional and the phase-field evolution equation retain the same structure as presented in Section 2, with all quantities consistently defined in the reference element volume (E_0). The finite element stiffness matrices of the damage and displacement subproblems ($\mathbf{K}^{FE}_{\phi,E_0}$, $\mathbf{K}^{FE}_{\mathbf{u},E_0}$) can be obtained by consistent linearization of the residual vector, ($\mathbf{R}^{FE}_{\phi,E_0}$, $\mathbf{R}^{FE}_{\mathbf{u},E_0}$). The residual vectors and the element stiffness matrices and can be expressed as:

$$\mathbf{K}^{FE}_{\phi,E_0} = \int_{E_0} \left\{ \left(\frac{G_c}{l_0} + 2\mathscr{H} \right) [\mathbf{N}_\phi]^T [\mathbf{N}_\phi] + G_c l_0 [\mathbf{B}_\phi]^T [\mathbf{B}_\phi] \right\} dE_0, \tag{39a}$$

$$\mathbf{R}^{FE}_{\phi,E_0} = -\int_{E_0} \left\{ \left(\frac{G_c}{l_0}\phi - 2(1-\phi)\mathscr{H} \right) [\mathbf{N}_\phi]^T + G_c l_0 ([\mathbf{B}_\phi])^T \nabla\phi \right\} dE_0, \tag{39b}$$

$$\mathbf{K}^{FE}_{\mathbf{u},E_0} = \int_{E_0} [\mathbf{B}_\mathbf{u}]^T : \frac{\partial \mathbf{P}^I}{\partial \mathbf{F}} : [\mathbf{B}_\mathbf{u}]\, dE_0, \tag{39c}$$

$$\mathbf{R}^{FE}_{\mathbf{u},E_0} = -\int_{E_0} \mathbf{P}^I : [\mathbf{B}_\mathbf{u}]\, dE_0, \tag{39d}$$

3.5. Implementation in ABAQUS using UEL and UMAT

We implement the proposed formulation in the commercial software ABAQUS (Standard). The entire simulation framework can be broadly classified into three stages as:

- Preprocessing
- Analysis

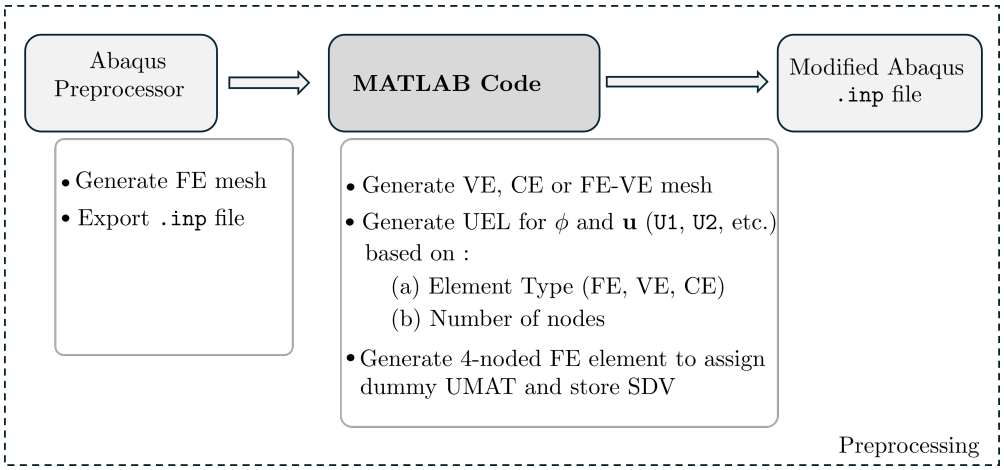

Figure 4: Schematic illustration of the Preprocessing stage in simulation workflow.

- Postprocessing

Fig. 4 illustrates the preprocessing workflow adopted to generate a modified Abaqus input (`.inp`) file starting from the Abaqus Preprocessor. The domain is first meshed using standard four-noded finite elements in the Abaqus Preprocessor and a raw `.inp` file is exported, which is subsequently processed using an in-house developed MATLAB code. This MATLAB code converts selected finite elements into virtual elements, generates cohesive elements along prescribed interfaces, and constructs polygonal virtual elements. The resulting modified `.inp` file consists of finite elements (FE), virtual elements (VE), and cohesive elements (CE), each assigned as different UEL types.

For matrix domains modeled using either VE alone or a hybrid combination of VE and FE, three overlapping layers of elements sharing identical nodal connectivity are created: the first two layers correspond to UEL elements storing ϕ and $\mathbf{u}$, respectively. Since Abaqus does not natively support visualization of UEL-based elements, a third layer consisting of standard four-noded finite elements with a dummy UMAT material is introduced solely for post-processing purposes. The UMAT material is modeled as a linear elastic material with very low stiffness and is used to store and visualize state variables (SDV) transferred from the UEL, such as $\boldsymbol{\sigma}$, $\boldsymbol{\varepsilon}$, $\mathscr{H}$, ϕ, etc., at the integration points of the four-noded UMAT elements.

Algorithm 1 presents the pseudocode for the implementation of the proposed framework using UEL and UMAT in Abaqus/Standard. The modified Abaqus `.inp` file is executed together with a Fortran 77 subroutine, which constructs the elemental tangent stiffness matrix (`AMATRX`) and the residual force vector (`RHS`) based on the element type and the active degrees of freedom. The global stiffness matrix is subsequently assembled by Abaqus, and the coupled governing equations are solved using an incremental–iterative Newton scheme within a staggered solution strategy [65]. The state variables associated with the UELs are stored at the integration points of a four-noded finite element layer assigned with a dummy UMAT material, enabling post-processing of results within Abaqus. Since Abaqus can only

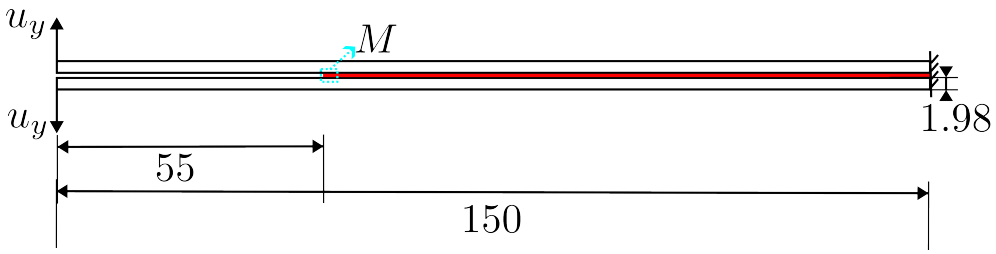

Figure 5: Schematic of the DCB specimen. All dimensions are in millimeters.

natively visualize quadrilateral elements, "*non-quadrilateral shaped*" polygonal virtual elements are represented as equivalent four-noded elements in the Abaqus postprocessor. To more accurately visualize the polygonal virtual elements, results from the Abaqus `.odb` file are exported to an Excel file using Python scripts, followed by additional post-processing in MATLAB.

4. Results and discussions

We now present numerical simulations that demonstrate the capability of the proposed framework to simulate typical damage mechanisms in composites through four representative examples, each validated against available experimental or numerical results. In Section 4.1, we simulate an interfacial crack propagating in a Double Cantilever Beam (DCB). Section 4.2 investigates whether a crack penetrates the opposite side of the interface or deflects along it. In Section 4.3, we analyze a crack that initially debonds along an interface and subsequently kinks into the matrix. Finally, in Section 4.4, we simulate multiple cracks nucleating in a hyperelastic composite consisting of a soft matrix and hard inclusions that are 3D printed.

All numerical simulations are carried out using the commercial finite element software Abaqus [25]. The element stiffness matrices, residual vectors, and load vectors are implemented through user-defined element (UEL) subroutines, and the results are mapped onto four-noded quadrilateral elements assigned with a dummy UMAT material having negligible elastic stiffness, as discussed in detail in Section 3.5. All simulations are executed on a Windows based PC equipped with an Intel(R) Core(TM) i9-9900KF CPU @ 3.60 GHz and 64 GB of RAM.

4.1. Interfacial crack in a Double Cantilever Beam (DCB) specimen

The problem of an interfacial crack propagating in a Double Cantilever Beam (DCB) specimen serves as a classical benchmark for simulating interfacial failure. We simulate delamination under Mode I loading conditions. The DCB specimen is manufactured using carbon (T300)/toughened epoxy (977-2) and consists of two limbs separated by a central crack of length 55 mm. Each limb has a length of 150 mm, a thickness of 1.98 mm, and an out-of-plane width of 20 mm [27]. One end of the specimen is fixed, while a symmetric vertical displacement is applied at the opposite end. A schematic of the DCB specimen and the associated boundary conditions is shown in Fig. 5. Plane strain conditions are assumed. We discretize the laminates using VEM meshes, with each laminate consisting of two layers.

Algorithm 1 Algorithmic structure for Abaqus implementation using UEL and UMAT

Input: Modified Abaqus `.inp` file consisting of UEL for FE, CE, VE and a dummy UMAT layer.
for Every UEL element (e.g., `U1`, `U2`, `U11`, etc.) **do**
    Identify active degrees of freedom ($\mathbf{u}$ or ϕ) and initialise $\mathbf{u}$, ϕ and History ($\mathscr{H}$).
    if ϕ is active **then**
        Compute History: $\mathscr{H}(\hat{\psi}_+^{elas}(\boldsymbol{\varepsilon})) = \max_{s\in[0,\tau]} \hat{\psi}_+^{elas}(\boldsymbol{\varepsilon}(s))$,
        if element is VE **then**
            Compute G, B, Π_ϕ^∇ using Eqs. 23a, 23b and 22a,
            Compute `AMATRX` using Eq. 26a,
            Compute `RHS` = `-AMATRX`$[\bar{\phi}] + \int_E 2\mathscr{H}[\Pi_\phi^\nabla]^T\, dE$,
        else if element is FE **then**
            Evaluate $[\mathbf{N}_\phi]$ and $[\mathbf{B}_\phi]$ at each integration point,
            Compute `AMATRX`, `RHS` using 39a and 39b using a Gauss Quadrature rule.
        end if
    end if
    if $\mathbf{u}$ is active **then**
        if element is VE **then**
            Compute $\mathbf{G}$, $\mathbf{B}$, $\Pi_{\mathbf{u},m}^\nabla$ using Eqs. 23c, 23d and 22b,
            Compute `AMATRX` using Eq. 26b,
            Compute `RHS` = `-AMATRX`$[\bar{\mathbf{u}}]$,
        else if element is FE **then**
            Evaluate $[\mathbf{N}_\mathbf{u}]$ and $[\mathbf{B}_\mathbf{u}]$ at each integration point,
            Compute `AMATRX`, `RHS` using 39c and 39d using a Gauss Quadrature rule,
        else if element is CE **then**
            Compute $\{\boldsymbol{\Delta}\}$ using Eq. 14,
            Compute `AMATRX` using Eq. 30,
            Compute `RHS` $= -\int_S [B^c]^T \begin{bmatrix} \frac{\partial \hat{\psi}^{int}}{\partial \Delta_t} \\ \frac{\partial \hat{\psi}^{int}}{\partial \Delta_n} \end{bmatrix} dS$.
        end if
    end if
end for
for every element in the dummy UMAT layer **do**
    Form the constitutive matrix of a linear elastic material with a very low stiffness.
    Store the state variables of the UEL (FE, VE, CE) such as $\boldsymbol{\sigma}$, $\boldsymbol{\varepsilon}$, $\mathscr{H}$, ϕ, etc. at the integration points of the element.
end for
Output: Element residual vector, (`RHS`) and tangent stiffness matrix (`AMATRX`).

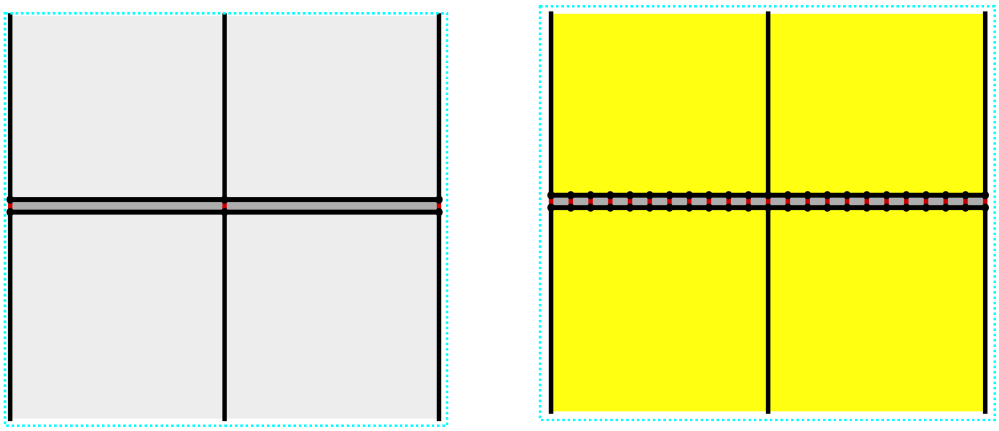

Figure 6: Zoomed-in view of the mesh at the region marked as 'M' in Fig. 5. Left- VEM mesh consisting of only four-noded elements. Right - VEM mesh with four-noded cohesive elements and 14-noded transition elements. The size of each cohesive element is 0.25 mm (left) and 0.025 mm (right).

Two mesh configurations are considered:

- **VEM HN 0 mesh**: The interface is discretized using four-noded cohesive elements and the laminates are discretized using four-noded quadrilateral elements.
- **VEM HN 10 mesh**: The interface is discretized using four-noded cohesive elements, while the layer adjacent to the interface in the laminates employs 14-noded elements. The upper layer of the laminate uses four-noded elements, resulting in ten "hanging" nodes at the interface.

This configuration highlights the capability of the VEM to handle non-matching meshes across interfaces, a feature not available in conventional FEM formulations. A zoomed-in view of the mesh near the DCB notch is shown in Fig. 6. The laminates are modeled as orthotropic materials, and their elastic properties, along with those of the interface, are listed in Table 1 and Table 2, respectively.

Table 1: Mechanical and fracture properties of laminates [27, 39, 98]

Property	Value
E_{xx}	150 GPa
$E_{yy} = E_{zz}$	11 GPa
$G_{xy} = G_{xz}$	6 GPa
G_{yz}	3.7 GPa
$\nu_{xy} = \nu_{xz}$	0.25
ν_{yz}	0.45
G_c	1 N/mm
l_0	0.025 mm

Table 2: Parameters of the PPR CZM used for the interface [27, 39, 98]

Parameter	Value
σ_n	60 MPa
σ_t	60 MPa
G_n	0.352 N/mm
G_t	0.352 N/mm
δ_n	0.015 mm
δ_t	0.015 mm
m	2
n	2

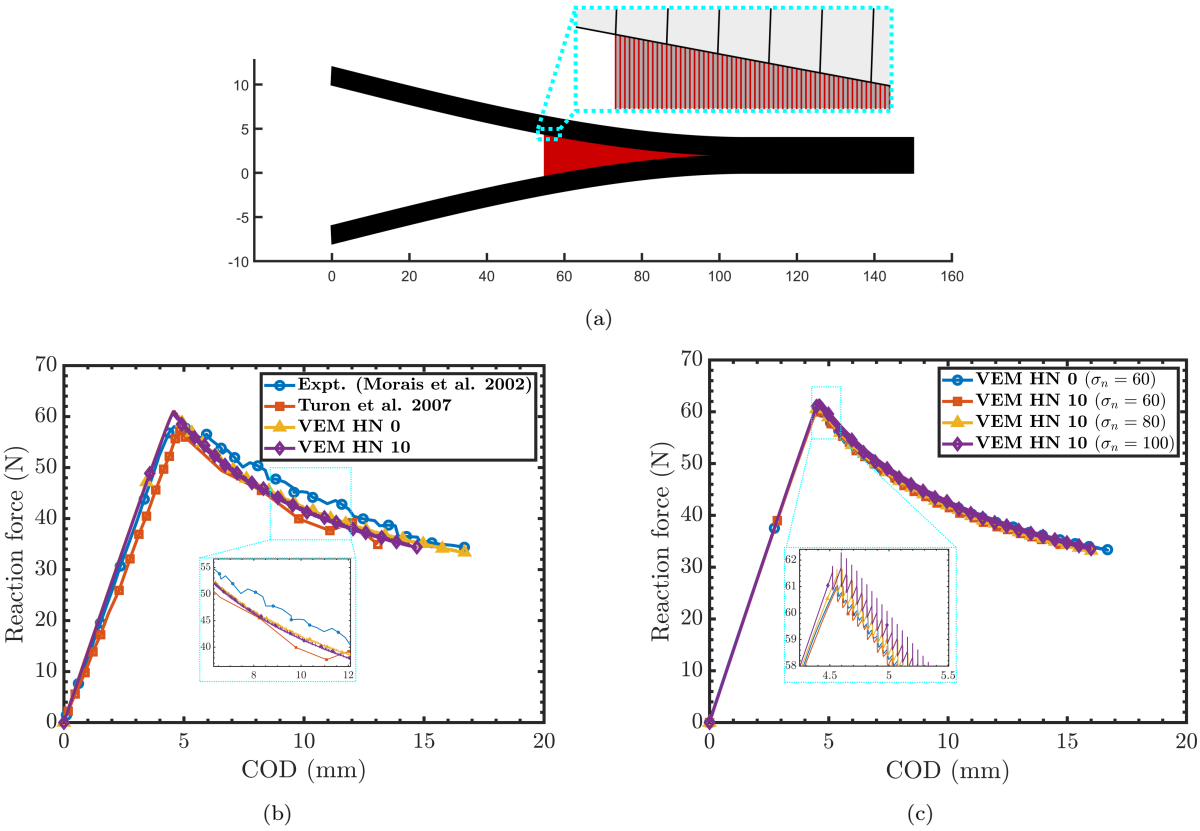

Figure 7: (a) Deformed plot of the DCB specimen (b) Vertical reaction force vs, Crack Opening Dispacement (COD) for the material properties listed in Table 1 and 2 (c) Vertical reaction force vs. COD for varying values of the normal strength of the interface (σ_n)

Figure 7a presents the final deformed configuration of the DCB specimen following pure interfacial failure, together with a zoomed-in view of the deformed mesh in the vicinity of the adhesive layer. Despite the presence of non-matching meshes across the interface, displacement continuity is preserved throughout the simulation. This behavior stems from the construction of the lowest-order VEM spaces, which enforce linear and continuous displacement fields along element boundaries, thereby ensuring kinematic compatibility without additional coupling constraints even under large interfacial separations.

The corresponding vertical reaction force versus Crack Opening Displacement (COD) response is shown in Fig. 7b. Both VEM discretizations (HN 0 and HN 10) exhibit excellent agreement with the experimental results reported in [27], accurately capturing the initial stiffness, peak load, and post-peak softening behavior. Minor oscillations observed in the post-peak regime are also present in the experimental data and are attributed to the high strength and brittle nature of the adhesive interface. These results demonstrate the robustness of the proposed VEM-based framework in modeling interfacial fracture while maintaining accuracy even in the presence of mismatched meshes.

Figure 7c illustrates the influence of interface strength on the load–displacement response of the DCB specimen. Three high normal interface strengths, $\sigma_n = 60$, 80, and 100, are considered. It is well known that the characteristic length scale of cohesive zone models scales inversely with the square of the interface strength [98]. Consequently, conventional FEM formulations would require prohibitively fine mesh refinement near the interface to accurately resolve damage evolution for such high-strength interfaces, resulting in a significant increase in computational cost. In contrast, the proposed VEM-based framework enables local refinement along the interface by introducing additional interface nodes without refining the surrounding laminates. This capability allows the framework to efficiently capture interfacial failure across a wide range of interface strengths while maintaining a coarse and computationally efficient discretization of the bulk domains, highlighting a key practical advantage of the proposed approach.

4.2. Penetration deflection studies

We next study the problem of a crack either penetrating or deflecting along an interface a classical benchmark for assessing the capability of a damage formulation to capture realistic crack trajectories in layered composites, where crack propagation results from a complex interplay between matrix and interface failure [23]. Alam et al. [3] conducted experiments to observe crack penetration or deflection as a function of the interface orientation. Figure 8 presents a schematic of the specimen. The sample has a thickness of 5.8 mm, with a notch introduced midway in one of the PMMA laminates. Another laminate is bonded to it at a prescribed orientation using an adhesive layer that forms the interface. Depending on the interface orientation, a crack initiated from the pre-existing notch may either propagate along the interface or penetrate into the adjoining laminate. The elastic and fracture properties of the PMMA laminates and the PPR cohesive zone model parameters of the adhesive interface are listed in Table 3 and Table 4, respectively. Plane strain conditions are assumed.

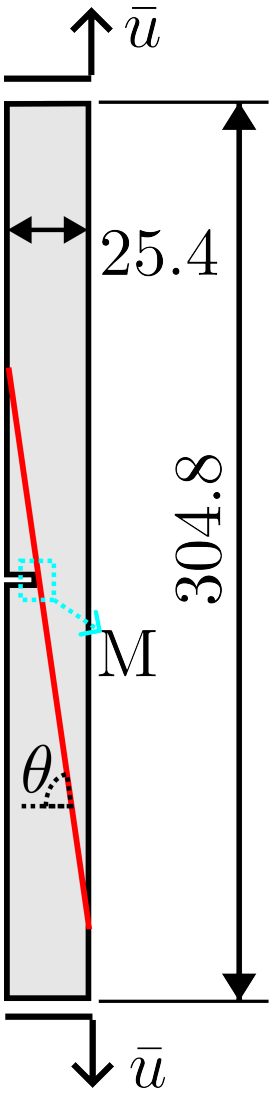

Figure 8: Schematic of the specimen used in the expt. [3]. The region marked as "M" is further illustrated in Fig. 9. All dimensions are in millimeters.

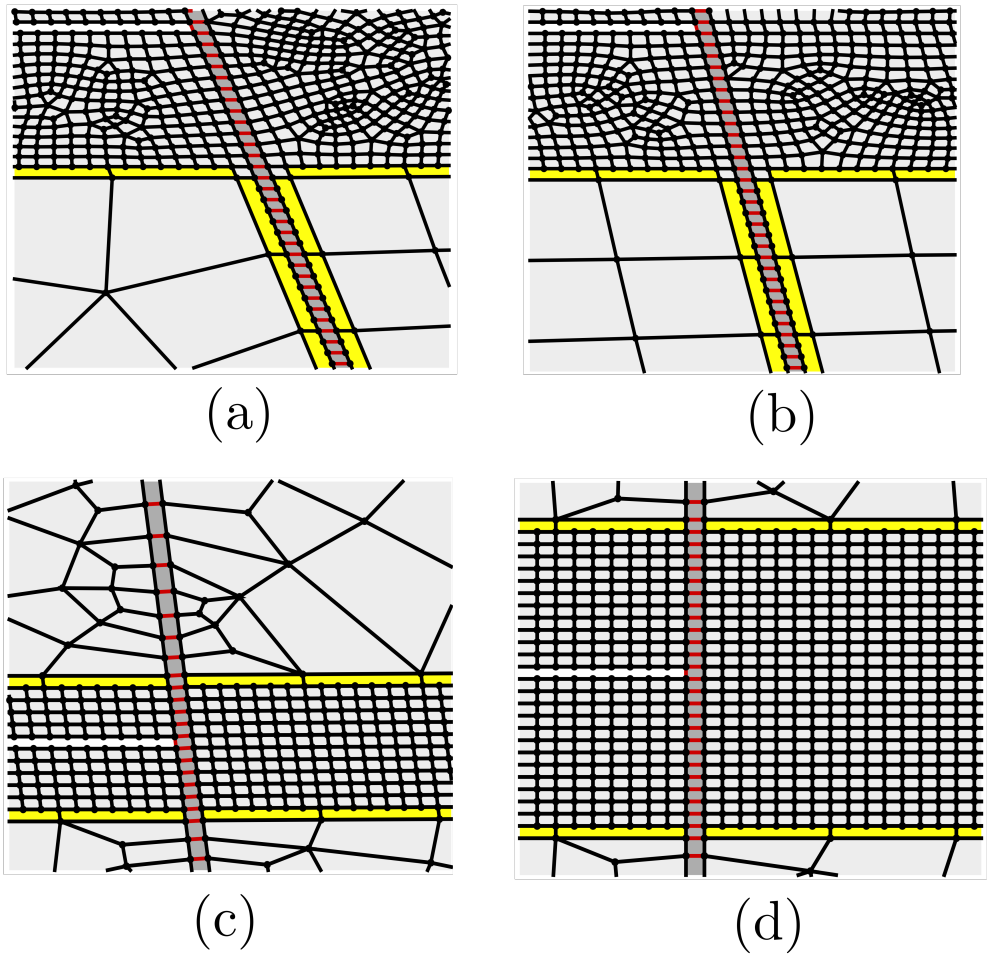

Figure 9: Zoomed-in view of the mesh near the notch (region marked as M in Fig. 8) with non-matching meshes at the interface and the laminate for the interface oriented at (a) 75° (b) 80° (c) 85° (d) 90°.

Table 3: Mechanical and fracture properties of PMMA laminates [3]

Property	Value
E	150 GPa
ν	0.37
G_c	0.621 N/mm
l_0	0.12 mm

Table 4: Parameters of the PPR CZM used for the interface [3]

Parameter	Value
σ_n	16.2 MPa
σ_t	16.2 MPa
G_n	0.3706 N/mm
G_t	0.3706 N/mm
δ_n	0.015 mm
δ_t	0.015 mm
m	2
n	2

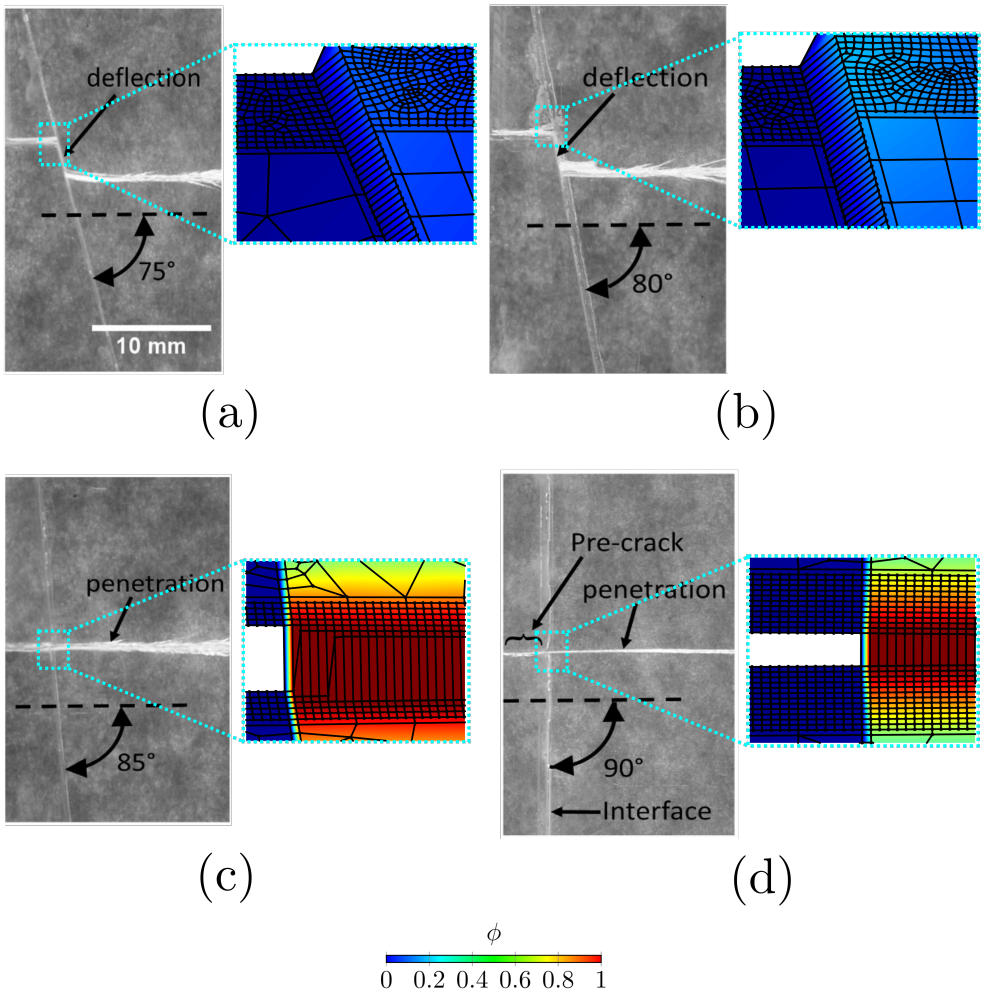

Figure 10: Experimental crack patterns [3] along with the simulated results for the interface oriented at (a) 75° (b) 80° (c) 85° (d) 90°

Figure 9 shows the discretization in the zoomed-in region "M" identified in Fig. 8. The PMMA matrix is discretized with four-noded virtual elements along with ten-noded transition virtual elements. Each of the ten-noded virtual element consist of six hanging nodes placed at a distance of $1l_0$ from the crack front [85]). The interface is discretized using four-noded cohesive elements. The transition elements enable a rapid transition from a fine mesh near the interface to a coarser mesh in the surrounding regions.

Figure 10 compares experimentally observed crack paths [3] with numerical predictions obtained using the proposed VEM-based framework for different interface orientations. For interface angles of 75° and 80°, the crack predominantly deflects along the interface. This behavior is characterized numerically by large deformation and elongation of the cohesive interface elements, while the phase-field damage variable ϕ in the adjacent laminate remains low. These results indicate that interfacial debonding is energetically favored over penetration into the bulk material for these orientations.

In contrast, for interface angles of 85° and 90°, the simulations show a clear transition from interfacial debonding to crack penetration into the laminate. This transition is marked by a pronounced increase in the phase-field damage variable ϕ within the bulk, consistent with experimentally observed penetration-dominated fracture. The ability of the proposed framework to capture this deflection–penetration transition across a range of interface orientations demonstrates its robustness in reproducing mixed-mode fracture mechanisms and highlights its capability to accurately predict competition between interfacial and bulk failure in composite materials.

4.3. Crack kinking out of an interface

We now consider the problem of a crack kinking out of an interface between a hard fiber and a soft matrix, as schematically illustrated in Fig. 11. The bottom face of the model is fixed, the lateral faces are constrained in the horizontal direction, and a vertical displacement is applied to the top face. The elastic and fracture properties of the matrix and inclusion, along with the PPR cohesive zone model parameters, are listed in Table 5 and Table 6, respectively. Plane strain conditions are assumed.

Table 5: Mechanical and fracture properties of the matrix and fiber (denoted by superscript 'm' and 'f' respectively) [96]

Property	Value
E^m	4 GPa
ν^m	0.4
E^f	40 GPa
ν^f	0.33
G_c^m	0.25 N/mm
l_0^m	0.0075 mm
G_c^f	0.4 N/mm
l_0^f	0.0075 mm

Table 6: Parameters of the PPR CZM used for the interface [96]

Parameter	Value
σ_n	120 MPa
σ_t	120 MPa
G_n	0.6 N/mm
G_t	0.6 N/mm
δ_n	0.2 mm
δ_t	0.2 mm
m	2
n	2

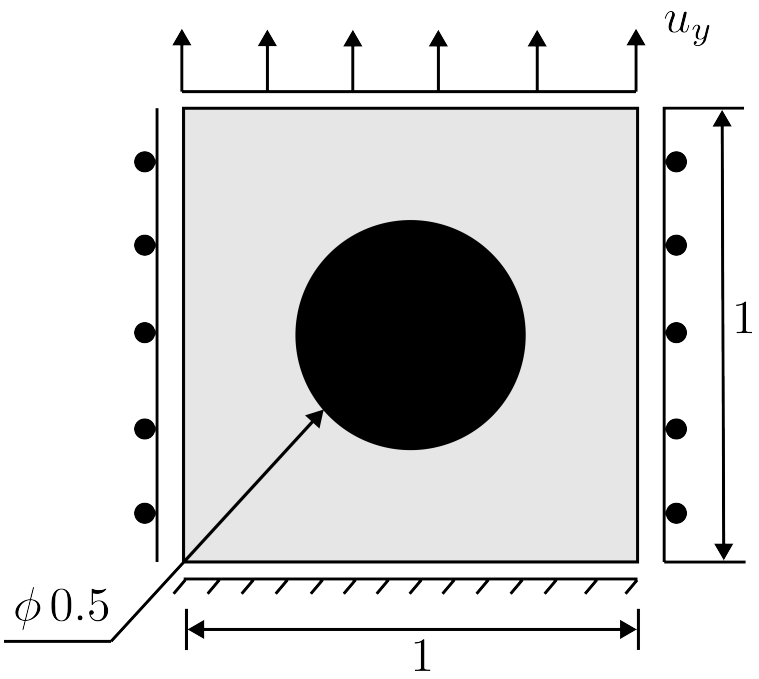

Figure 11: A mesoscale representation of a hard fiber embedded in a soft matrix. All dimensions are in millimeters.

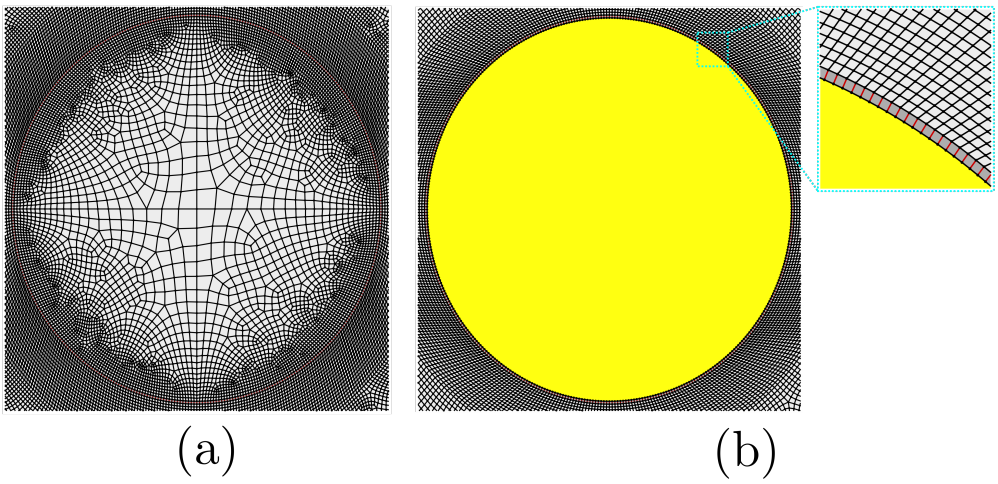

Figure 12: Comparison between FEM and VEM discretizations of the inclusion (a) FEM - inclusion is discretized with 5810 four-noded elements (b) VEM - inclusion discretized with a single polygonal element with 420 nodes.

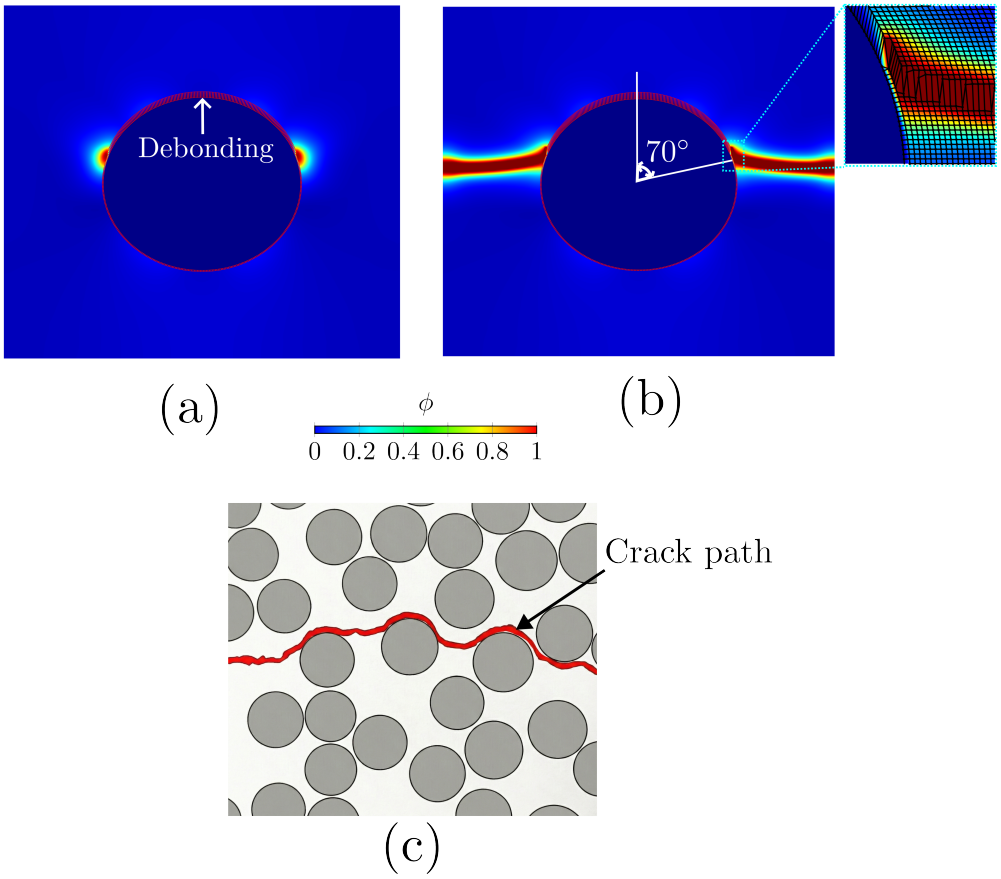

Figure 13: Stages of crack kinking out of the fiber-matrix interface (a) Initial debonding (b) Crack kinking out of the interface at around 70° (c) Experimentally observed crack patterns (digitized) [76]

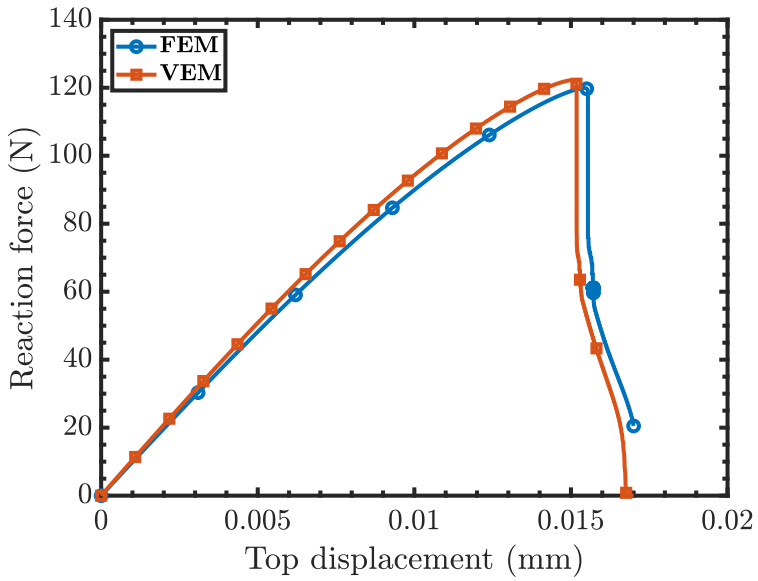

Figure 14: Vertical reaction force vs. vertical displacement for the FEM mesh and VEM mesh

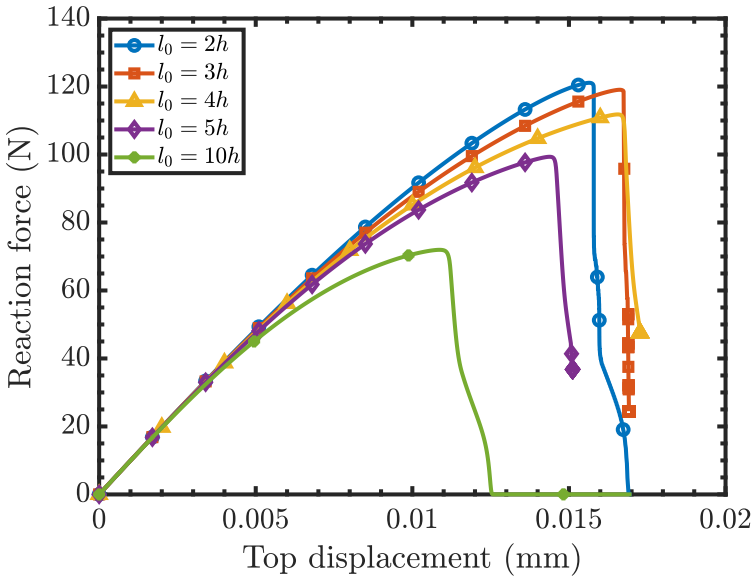

Figure 15: Reaction force versus top displacement for different values of the phase-field length scale parameter relative to the characteristic element size, $l_0/h = 2, 3, 4, 5$, and 10. Here $h = 0.00375\,mm$ denotes the characteristic mesh size.

We consider two types of discretization as shown in Fig. 12. Fig. 12a shows the FEM mesh, while figure Fig. 12b shows the VEM mesh. In both these cases four-noded cohesive elements are used at the interface between matrix and fiber. The mesh near the interface has an element size (h) of 0.00375 mm to accurately capture the steep stress and damage gradients during crack propagation along the interface or into the matrix. Since the fiber is ten times stiffer than the matrix, the crack does not kink into the fiber. However, when using FEM, the fine mesh required in the adjacent matrix and interface results in an inefficient discretization of the fiber, as only quadrilateral and triangular elements are permitted. This inefficiency is evident in Fig. 12: the FEM mesh required 5810 four-noded elements to discretize the fiber. In contrast, the VEM allows any polygonal shape, enabling the inclusion to be modeled with a single polygonal element containing 420 nodes without the need to compute shape functions.

Figure 13 illustrates the crack initiation and propagation mechanisms captured using the VEM mesh with the inclusion modeled as a single polygonal element. Crack initiation is first observed as interfacial debonding along the fiber–matrix interface, driven by the high stiffness and fracture toughness mismatch between the two phases. As loading progresses, the interface crack arrests once the energy release rate along the interface becomes insufficient to sustain further propagation.

Subsequently, a secondary crack nucleates within the surrounding matrix and the crack kinks away from the interface, propagating through the matrix at an angle of approximately 70° with respect to the vertical axis. This crack deflection behavior is consistent with experimentally observed fracture paths in fiber-reinforced composites and reflects the competition between interfacial fracture resistance and bulk matrix toughness [76]. The results

demonstrate that the proposed framework accurately captures mixed-mode crack deflection without even with fibers modeled as single polygonal element with arbitrarily large number of nodes.

Figure 14 compares the vertical reaction force–displacement responses obtained using FEM and VEM discretizations. The initial elastic stiffness predicted by both methods is nearly identical, indicating consistent representation of the global structural response. The peak load and subsequent softening behavior are also well captured by the VEM formulation, closely matching the FEM results.

Notably, the VEM model represents the rigid inclusion using a single 420-noded polygonal element, whereas the FEM model requires 5810 quadrilateral elements to discretize the same region. Despite this drastic reduction in mesh complexity, the VEM achieves comparable accuracy in both peak load and post-peak response. This highlights a key advantage of the VEM framework, it enables accurate fracture prediction with substantially fewer degrees of freedom while offering superior geometric flexibility for modeling rigid or complex-shaped inclusions.

To assess the sensitivity of the proposed framework with respect to the phase-field length scale parameter, simulations were performed by varying the ratio l_0/h, where h denotes the characteristic element size in the refined fracture zone. The mesh size h is chosen to be 0.00375 mm according to FEM simulations in [96]. Figure 15 shows the reaction force versus applied vertical displacement at the top for $l_0/h = 2, 3, 4, 5$, and 10.

The results indicate that smaller values of l_0/h lead to a sharper post-peak response and higher peak loads, whereas increasing l_0/h results in a more diffused damage zone and a reduction in the peak reaction force. For excessively large values of $l_0/h = 5h, 10h$, premature softening and variations in crack kinking angles were observed. These findings highlight the regularization role of the phase-field length scale and emphasize the necessity of selecting an appropriate l_0/h ratio to ensure physically consistent and mesh-independent results.

Table 7: Comparison of computational cost between FEM and VEM discretizations.

Method	Degrees of freedom	Total CPU time (s)
FEM	70,416	25,118
VEM	65,796	11,922
Reduction (%)	6.56	52.54

Table 7 compares the computational performance of the FEM and VEM discretizations for the same fracture problem. The VEM-based formulation achieves a reduction of approximately 6.6% in the total number of degrees of freedom compared to the FEM discretization, while yielding a substantially larger reduction of about 52.5% in total CPU time. This pronounced decrease in computational cost can be attributed to the ability of VEM to efficiently represent rigid or nearly rigid inclusions using single polygonal elements with a large number of nodes, thereby reducing the overall system size and improving solver efficiency. Moreover, unlike conventional FEM, the VEM formulation avoids explicit numerical integration over element interiors and does not require looping over multiple integration points,

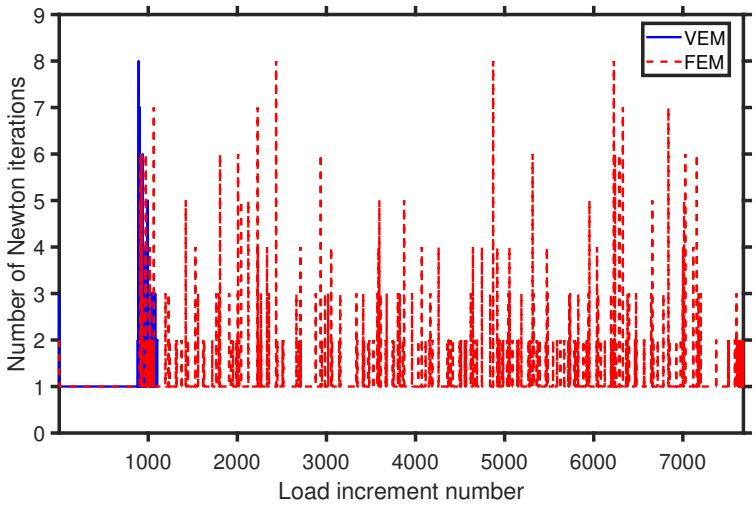

Figure 16: Evolution of the number of Newton iterations per load increment for the FEM and VEM discretizations.

which further enhances computational efficiency. These results highlight the advantages of the proposed VEM framework, particularly for composite structures characterized by strong material contrast and complex geometries.

Figure 16 compares the evolution of the number of Newton iterations per load increment for the FEM and VEM discretizations. The FEM formulation requires a significantly larger number of load increments (approximately seven times more than VEM) and exhibits frequent spikes in the Newton iteration count, particularly during crack initiation and propagation. This behavior arises because, as cracks initiate and evolve, finite elements in the vicinity of the crack become increasingly distorted, leading to difficulties in achieving convergence within the prescribed number of Newton iterations. Consequently, the Abaqus solver automatically reduces the time increment, resulting in a substantial increase in the total number of load increments.

In contrast, the VEM-based formulation is inherently robust with respect to element distortion, as it does not rely on an explicit mapping of element geometry to a reference (parent) element. As a result, the VEM formulation converges with fewer Newton iterations per increment and requires significantly fewer total load increments to reach complete failure. This improved convergence behavior, combined with the reduced number of degrees of freedom reported in Table 7, directly contributes to the pronounced reduction in total simulation time observed for the VEM framework. Fewer nonlinear iterations and load increments result in a smaller number of global stiffness assemblies and computation of tangent stiffness matrices, thereby enhancing overall computational efficiency.

4.4. Crack propagating in hyperelastic composites

The phase-field formulation presented in Section 2 is developed within the framework of infinitesimal strain kinematics and is employed throughout this work for small-deformation fracture simulations. To model fracture in hyperelastic composites undergoing large deforma-

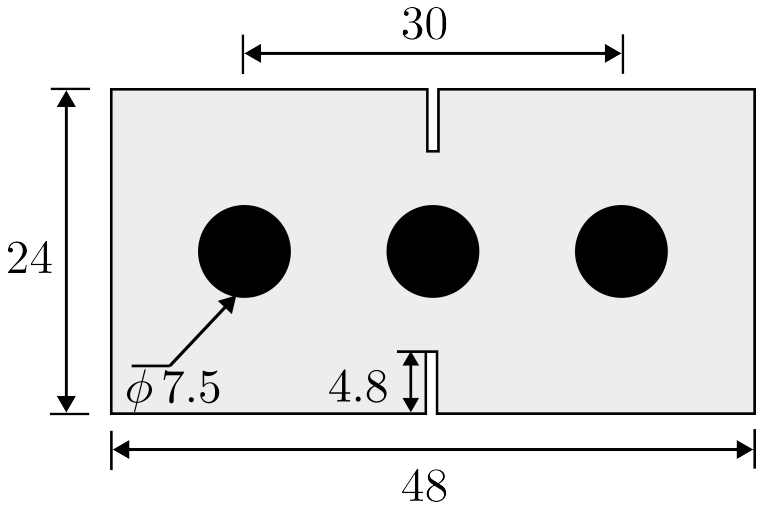

Figure 17: Schematic of the specimen. All dimensions are in millimeters.

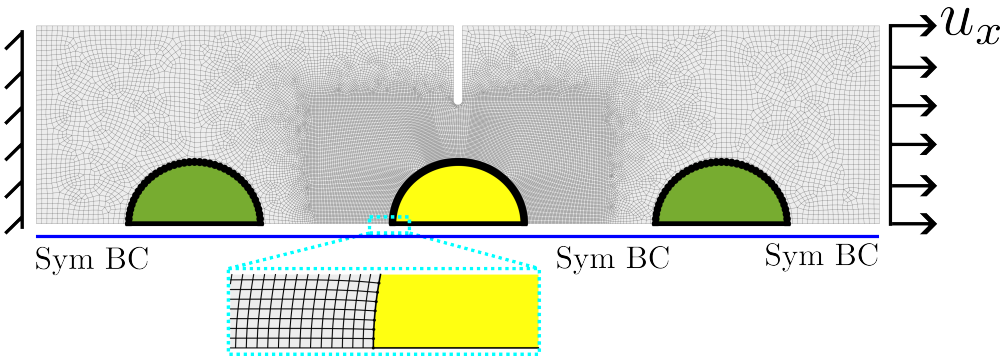

Figure 18: Mesh and the boundary conditions. The inclusions are discretized with a single polygonal virtual element while the matrix is discretized with four-noded finite elements.

tions, this framework is extended to finite deformation kinematics following the formulation proposed in Section 3.4.1.

We now consider the problem of crack propagation in a hyperelastic composite, experimentally and numerically investigated in [83]. The specimen is 3D printed using a soft elastomeric TangoBlackPlus (TP) material forming the matrix and a stiff VeroWhite (VW) material forming the inclusions. The specimen geometry is illustrated in Fig. 17. In the experiments [83], several configurations were tested by varying the distance between inclusions and the notch length. In this study, we analyze the N20D30 specimen, where the initial notch length equals 20% of the specimen width (4.8 mm), and the center-to-center distance between the outermost inclusions is 30 mm. The specimen is subjected to tension by pulling one end while fixing the other.

The discretization of the N20D30 specimen and the applied boundary conditions are shown in Fig. 18. Symmetry boundary conditions are imposed to reduce the computational cost. A slight asymmetry is introduced by horizontally shifting the central inclusion by 0.024 mm to capture geometric imperfections resulting from the 3D printing process [83].

Table 8: Material properties used in the simulation [83, 106, 38]. Superscript 'm' represents the matrix (TP) and 'i' represents the inclusion (VW).

Property	Value
μ^m	0.24 MPa
ν^m	0.499
G_c^m	0.7 N/mm
l_0^m	0.8 mm
μ^i	714 MPa
ν^i	0.4
G_c^i	1 N/mm
l_0^i	0.8 mm

Both finite elements and virtual elements are employed in the numerical model. Since the four-noded finite elements exhibit linear displacement and damage variations along their boundaries, they can be seamlessly coupled with first-order virtual elements. Accordingly, the TP matrix is discretized using four-noded plane stress finite elements, whereas each inclusion is modeled using a single polygonal virtual element. The central inclusion comprises one polygonal element with 165 nodes, while the other two inclusions each contain a single polygonal element with 41 nodes. The VEM-FEM hybrid discretization strategy has been discussed in detail in Section 3.4.

The soft TP matrix material is modeled using a Neo-Hookean formulation, which undergoes finite deformation prior to brittle fracture, whereas the VW inclusions are modeled as linear elastic materials that fail in a brittle manner. Since none of the experimental specimens reported in [83] exhibited interfacial debonding, the interface is assumed to be sufficiently strong relative to the surrounding matrix, and interfacial debonding is therefore not modeled in the current simulation. The material parameters used in the simulations are listed in Table 8. The TP material is nearly incompressible, with $\nu^m = 0.499$, while the stiff VW inclusions are approximately 3000 times stiffer than the TP matrix. An artificial viscosity of 0.001 is introduced to mitigate numerical convergence issues [83, 106, 38].

Figure 19 illustrates the stages of crack propagation in the hyperelastic composite. The figures on the left show the experimentally observed crack paths [83], while those on the right present the corresponding simulation results. The phase-field variable is plotted on the deformed configuration at different stretch ratios, defined as $\Lambda = \frac{\text{Final length}}{\text{Initial length}}$. Regions where the phase-field damage variable exceeds 0.9 are omitted for clarity.

At a stretch ratio of approximately $\Lambda = 1.1500$, the primary notch begins to open. Due to the hyperelastic nature of the soft TP matrix, the crack tip blunts as the crack emanates from the notch, causing the primary crack to arrest near the inclusion at $\Lambda = 1.3878$. The numerically predicted stretch ratio at arrest agrees well with experimental observations. Once the crack tip becomes significantly blunted by the nonlinear elastic deformation ahead of the front, a secondary crack nucleates between the inclusions at $\Lambda \approx 1.4262$, which is about 2.6% lower than the experimental value. This deviation is likely due to time-dependent stress

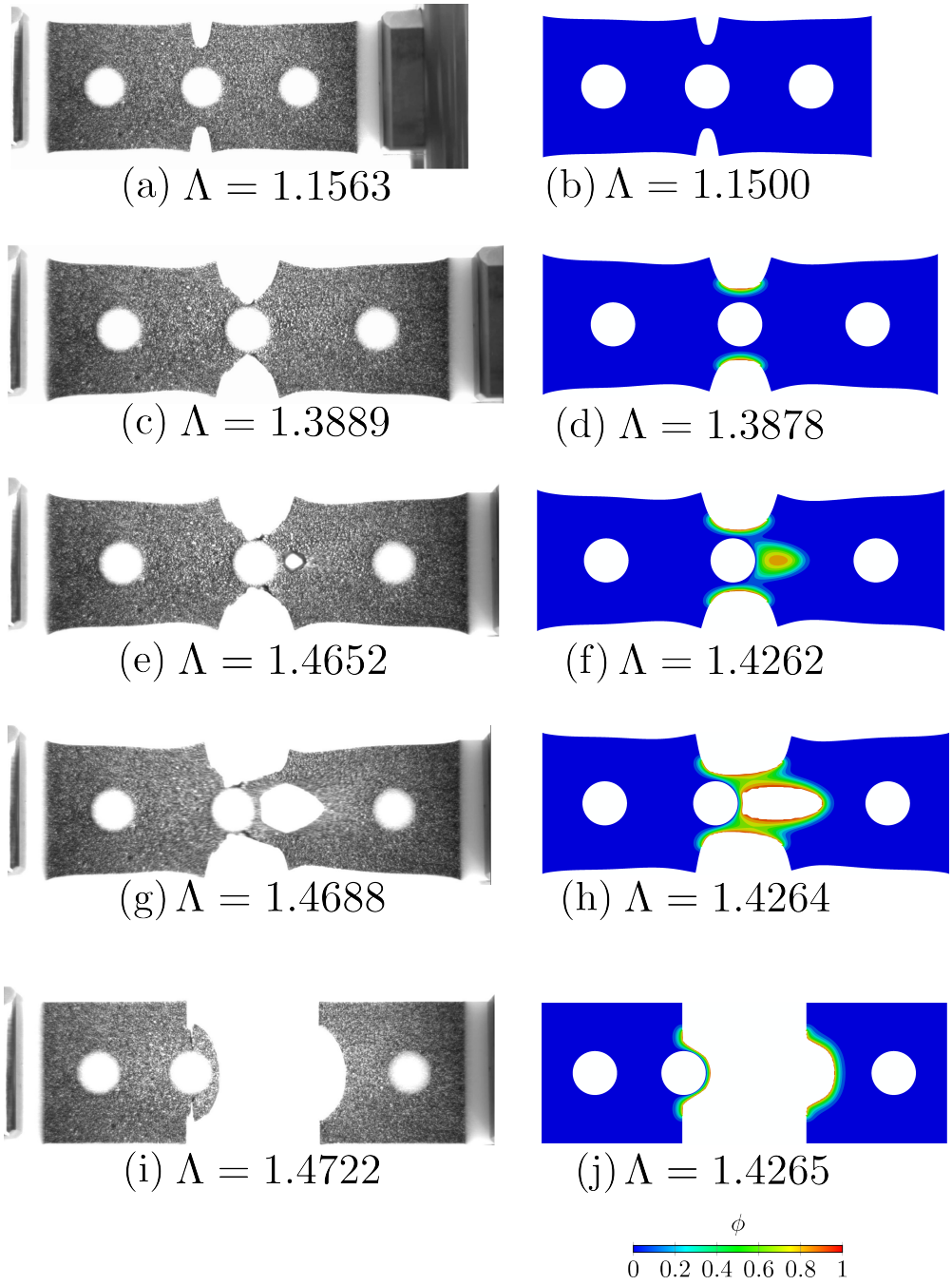

Figure 19: Stages of crack propagation in hyperelastic composite. Experimental observations (left) [83] and simulation results (right). $\Lambda = \frac{\text{Final length}}{\textbf{Initial length}}$

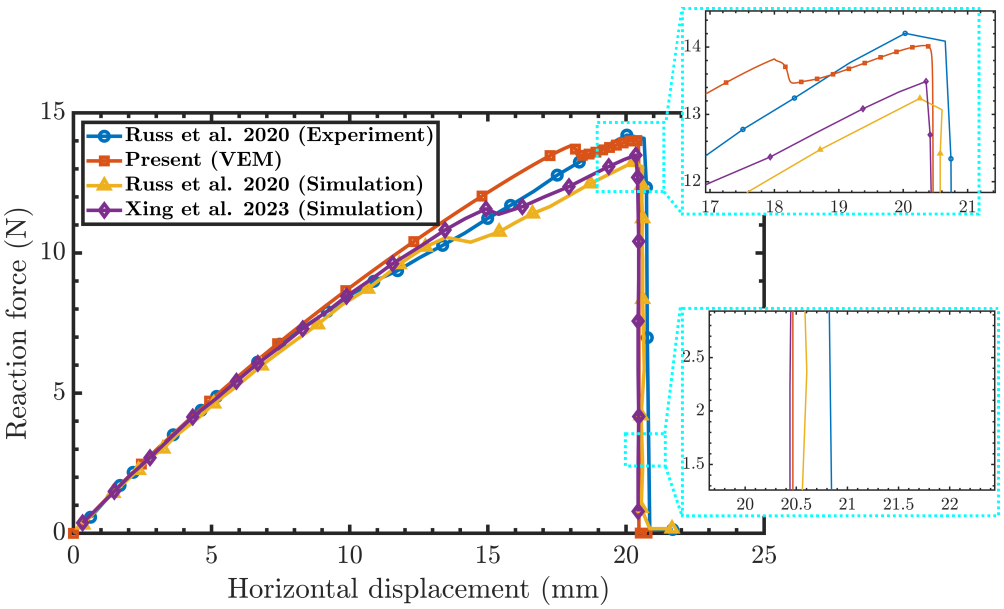

Figure 20: Horizontal reaction force vs. horizontal displacement

relaxation in the TP material, which is not accounted for in the present model. The primary and secondary cracks subsequently coalesce to form a continuous crack that fully separates the specimen at $\Lambda = 1.4265$, approximately 3% below the experimentally measured value.

Figure 20 presents the horizontal reaction force as a function of the applied horizontal displacement, comparing the present VEM-FEM based results with experimental data [83] and FEM-based numerical simulations from the literature. The initial non-linear response shows excellent agreement among all approaches, indicating that the proposed formulation accurately captures the effective stiffness of the composite prior to damage initiation. The peak reaction force is also well predicted, and the overall load–displacement trajectory up to failure closely follows the experimental response, with the deviation in displacement at failure remaining within approximately 2%.

The abrupt post-peak force drop corresponds to unstable crack propagation through the hyperelastic matrix in the presence of stiff inclusions. The ability of the proposed framework to accurately reproduce both the peak load and the sudden loss of load-carrying capacity suggests that the essential fracture mechanisms such as stress redistribution around rigid inclusions and crack localization are well captured. Notably, this level of agreement is achieved while modeling each inclusion using a single polygonal virtual element with a large number of nodes, demonstrating that the VEM can accurately resolve complex crack–inclusion interactions without the need for highly refined, conforming finite element meshes.

5. Conclusions

This study presented a robust discretization framework for simulating failure in composite structures by coupling the phase-field and cohesive-zone models within the Virtual

Element Method (VEM) formulation. The phase-field model was employed to capture bulk fracture, while the cohesive-zone model represented interfacial debonding. The performance and versatility of the proposed framework were demonstrated through four benchmark problems, validated against experimental and numerical results. The key conclusions drawn from this study are as follows:

- The lowest-order VEM can be seamlessly integrated with four-noded linear cohesive elements, enabling the construction of non-uniform meshes across interfaces and thereby providing significant flexibility in mesh design.
- For interfacial fracture simulations, the VEM allows highly refined discretization within the cohesive zone while maintaining coarse meshes in the adjoining laminates. This capability facilitates efficient modeling of high-strength interfaces without requiring the prohibitively dense meshes demanded by conventional FEM.
- The VEM successfully reproduces experimentally observed crack penetration and deflection patterns at composite interfaces using non-matching meshes in both the bulk and interface regions, confirming its robustness for heterogeneous discretizations.
- Rigid inclusions can be represented as single polygonal VEM elements containing several hundred nodes (up to 420 in this study) without compromising the accuracy of crack-kinking angles or reaction–displacement responses when compared to FEM.
- The compatibility between the lowest-order virtual elements and four-noded displacement-based finite elements enables a hybrid discretization strategy. This approach allows the VEM to be applied selectively in regions with complex mesh topologies, efficiently capturing multiple crack nucleation and coalescence phenomena in hyperelastic composites. The numerical predictions show excellent agreement with experimental crack paths and load–displacement responses.
- The proposed VEM-based formulation exhibits superior convergence characteristics compared to FEM, requiring significantly fewer load increments, particularly during crack initiation and propagation. This improved robustness with respect to element distortion, together with the reduced number of degrees of freedom, leads to a substantial reduction in global stiffness assemblies and tangent stiffness computations, thereby resulting in a significant reduction in computational cost.

Overall, the results highlight the potential of the Virtual Element Method as a flexible and computationally efficient framework for modeling fracture processes in composite materials, particularly in the presence of strong material mismatch, non-matching interfaces, and complex geometries. Notwithstanding these advantages, the following limitations and directions for future research are identified:

- In Section 4.4, where the hyperelastic matrix undergoing finite deformation is discretized using finite elements, convergence difficulties were encountered in Abaqus(Standard),

particularly during secondary crack nucleation. Similar challenges have been reported in the literature [93]. To ensure numerical convergence, the default artificial stabilization procedures available in Abaqus(Standard) were employed. These difficulties are likely associated with ill-conditioning of finite element stiffness matrices arising from severe element distortion [33, 11, 42, 43]. A systematic investigation of the conditioning of global tangent matrices for different discretization strategies constitutes an important direction for future study.

- The present VEM framework is restricted to two-dimensional fracture analyses in composite structures. An extension to three-dimensional problems would enable the investigation of out-of-plane crack growth and complex crack surface morphologies. Furthermore, the incorporation of adaptive mesh refinement strategies within the VEM framework could further enhance computational efficiency and accuracy in large-scale simulations.

- The composite matrix considered in this study exhibits brittle fracture behavior, which is representative of epoxy-based composite materials. However, cementitious composites such as concrete display quasi-brittle behavior characterized by pronounced softening prior to complete failure and often involve aggregates with highly irregular geometries. The proposed framework is well suited to address these challenges by modeling aggregates as single virtual elements and by incorporating quasi-brittle fracture models for the cementitious matrix, thereby offering a promising avenue for future applications.

References

[1] Ahmadi, M., Sadighi, M., Hosseini-Toudeshky, H., 2022. Microstructure-based deformation and fracture modeling of particulate reinforced composites with ordinary state-based peridynamic theory. Composite Structures 279, 114734.

[2] Al-Azzawi, A.S., Kawashita, L., Featherston, C., 2019. A modified cohesive zone model for fatigue delamination in adhesive joints: numerical and experimental investigations. Composite Structures 225, 111114.

[3] Alam, M., Parmigiani, J.P., Kruzic, J.J., 2017. An experimental assessment of methods to predict crack deflection at an interface. Engineering Fracture Mechanics 181, 116–129.

[4] Alessi, R., Freddi, F., 2017. Phase-field modelling of failure in hybrid laminates. Composite Structures 181, 9–25.

[5] Alfano, G., 2006. On the influence of the shape of the interface law on the application of cohesive-zone models. Composites Science and Technology 66, 723–730.

[6] Allegri, G., 2020. A unified formulation for fatigue crack onset and growth via cohesive zone modelling. Journal of the Mechanics and Physics of Solids 138, 103900.

[7] Ambati, M., Gerasimov, T., De Lorenzis, L., 2015. A review on phase-field models of brittle fracture and a new fast hybrid formulation. Computational Mechanics 55, 383–405.

[8] Amor, H., Marigo, J.J., Maurini, C., 2009. Regularized formulation of the variational brittle fracture with unilateral contact: Numerical experiments. Journal of the Mechanics and Physics of Solids 57, 1209–1229.

[9] Aoki, R., Higuchi, R., Yokozeki, T., 2021. Fatigue simulation for progressive damage in cfrp laminates using intra-laminar and inter-laminar fatigue damage models. International Journal of Fatigue 143, 106015.

[10] Artioli, E., Beirão da Veiga, L., Verani, M., 2020. An adaptive curved virtual element method for the statistical homogenization of random fibre-reinforced composites. Finite Elements in Analysis and Design 177, 103418. doi:https://doi.org/10.1016/j.finel.2020.103418.

[11] Badri, M., Rastiello, G., Foerster, E., 2021. Preconditioning strategies for vectorial finite element linear systems arising from phase-field models for fracture mechanics. Computer Methods in Applied Mechanics and Engineering 373, 113472.

[12] Benedetto, M.F., Caggiano, A., Etse, G., 2018. Virtual elements and zero thickness interface-based approach for fracture analysis of heterogeneous materials. Computer Methods in Applied Mechanics and Engineering 338, 41–67.

[13] Bieniaś, J., Dębski, H., Surowska, B., Sadowski, T., 2012. Analysis of microstructure damage in carbon/epoxy composites using fem. Computational Materials Science 64, 168–172.

[14] van den Bosch, M.J., Schreurs, P.J., Geers, M.G., 2006. An improved description of the exponential Xu and Needleman cohesive zone law for mixed-mode decohesion. Engineering Fracture Mechanics 73, 1220–1234. doi:10.1016/J.ENGFRACMECH.2005.12.006.

[15] Bourdin, B., Francfort, G.A., Marigo, J.J., 2000. Numerical experiments in revisited brittle fracture. Journal of the Mechanics and Physics of Solids 48, 797–826.

[16] Bui, T.Q., Hu, X., 2021. A review of phase-field models, fundamentals and their applications to composite laminates. Engineering Fracture Mechanics 248, 107705.

[17] Böhm, C., Hudobivnik, B., Marino, M., Wriggers, P., 2021. Electro-magneto-mechanically response of polycrystalline materials: Computational homogenization via the virtual element method. Computer Methods in Applied Mechanics and Engineering 380, 113775. doi:https://doi.org/10.1016/j.cma.2021.113775.

[18] Cangiani, A., Manzini, G., Russo, A., Sukumar, N., 2015. Hourglass stabilization and the virtual element method. International Journal for Numerical Methods in Engineering 102, 404–436. doi:10.1002/nme.4854.

[19] Cao, E., Dong, Z., Jia, B., Huang, H., 2025. Inverse design of isotropic auxetic metamaterials via a data-driven strategy. Materials Horizons .

[20] Chen, J., Dai, Y., Jia, B., Zheng, Y., Huang, H., 2025. Effect of forced assembly gap on the fatigue behavior of aluminium alloy multi-bolted joints under random loading. International Journal of Fatigue , 109344.

[21] Cheng, Z.Q., Liu, H., Tan, W., 2024. Advanced computational modelling of composite materials. Engineering Fracture Mechanics , 110120.

[22] Cheng, Z.Q., Tan, W., Xiong, J.J., 2022. Modelling pre-fatigue, low-velocity impact and post-impact fatigue behaviours of composite helicopter tail structures under multipoint coordinated loading spectrum. Thin-Walled Structures 176, 109349.

[23] Clegg, W., Kendall, K., Alford, N.M., Button, T., Birchall, J., 1990. A simple way to make tough ceramics. Nature 347, 455–457.

[24] Das, S., Sharma, S., Ramaswamy, A., Roy, D., Reddy, J., 2021. A geometrically inspired model for brittle damage in compressible elastomers. Journal of Applied Mechanics 88.

[25] Dassault Systèmes Simulia Corp., 2013. Abaqus/Standard User's Manual, Version 2024. Providence, RI, USA.

[26] Dau, F., Girardot, J., Le, B.D., 2016. A promising way to model damage in composite and dry fabrics using a discrete element method (dem). Applied Mechanics and Materials 828, 119–136.

[27] De Morais, A., De Moura, M., Marques, A., De Castro, P., 2002. Mode-i interlaminar fracture of carbon/epoxy cross-ply composites. Composites Science and Technology 62, 679–686.

[28] Deng, H., Yan, B., Koyanagi, J., 2023. Improved xfem for 3d interfacial crack modeling. Mechanics of Materials 186, 104811.

[29] Ding, X., Gu, Z., Hou, X., Xia, M., Ismail, Y., Ye, J., 2023. Effects of defects on the transverse mechanical response of unidirectional fibre-reinforced polymers: Dem simulation and deep learning prediction. Composite Structures 321, 117301.

[30] Divse, V., Marla, D., Joshi, S.S., 2023. Progressive damage analysis in an open hole compression of frp laminates including fiber kinking and pre-existing damage. Composites Part A: Applied Science and Manufacturing 169, 107523.

[31] Ebadi-Rajoli, J., Akhavan-Safar, A., Hosseini-Toudeshky, H., Da Silva, L., 2020. Progressive damage modeling of composite materials subjected to mixed mode cyclic loading using cohesive zone model. Mechanics of Materials 143, 103322.

[32] Ekhtiyari, A., Shokrieh, M.M., 2022. A novel rate-dependent cohesive zone model for simulation of mode i dynamic delamination in laminated composites. Composite Structures 281, 114962.

[33] Farrell, P., Maurini, C., 2017. Linear and nonlinear solvers for variational phase-field models of brittle fracture. International Journal for Numerical Methods in Engineering 109, 648–667.

[34] Francfort, G.A., Marigo, J.J., 1998. Revisiting brittle fracture as an energy minimization problem. Journal of the Mechanics and Physics of Solids 46, 1319–1342.

[35] Freed, Y., Banks-Sills, L., 2008. A new cohesive zone model for mixed mode interface fracture in bimaterials. Engineering Fracture Mechanics 75, 4583–4593.

[36] Frémond, M., Nedjar, B., 1996. Damage, gradient of damage and principle of virtual power. International journal of solids and structures 33, 1083–1103.

[37] Gatta, C., Pingaro, M., Addessi, D., Trovalusci, P., 2024. A coupled virtual element-interface model for analysis of fracture propagation in polycrystalline composites. Computer Methods in Applied Mechanics and Engineering 432, 117383.

[38] George, D., Konica, S., Masters, I., Hossain, M., 2025. A phase field formulation for modelling fracture of nearly incompressible hyperelastic materials. Computer Methods in Applied Mechanics and Engineering 436, 117696.

[39] Goyal, V.K., Johnson, E.R., Davila, C.G., 2004. Irreversible constitutive law for modeling the delamination process using interfacial surface discontinuities. Composite Structures 65, 289–305.

[40] Hansen-Dörr, A.C., de Borst, R., Hennig, P., Kästner, M., 2019. Phase-field modelling of interface failure in brittle materials. Computer Methods in Applied Mechanics and Engineering 346, 25–42.

[41] Heidari-Rarani, M., Sayedain, M., 2019. Finite element modeling strategies for 2d and 3d delamination propagation in composite dcb specimens using vcct, czm and xfem approaches. Theoretical and Applied Fracture Mechanics 103, 102246.

[42] Heister, T., Mang, K., Wick, T., 2021. Schur-type preconditioning of a phase-field fracture model in mixed form. PAMM 21, e202100065.

[43] Hesch, C., Gil, A., Ortigosa, R., Dittmann, M., Bilgen, C., Betsch, P., Franke, M., Janz, A., Weinberg, K., 2017. A framework for polyconvex large strain phase-field methods to fracture. Computer Methods in Applied Mechanics and Engineering 317, 649–683.

[44] Hu, X., Chen, B., Tirvaudey, M., Tan, V., Tay, T., 2016. Integrated xfem-ce analysis of delamination migration in multi-directional composite laminates. Composites Part A: Applied Science and Manufacturing 90, 161–173.

[45] Huang, Y.j., Zheng, Z.s., Yao, F., Zeng, C., Zhang, H., Natarajan, S., Xu, S.l., 2024. Arbitrary polygon-based csfem-pfczm for quasi-brittle fracture of concrete. Computer Methods in Applied Mechanics and Engineering 424, 116899.

[46] Hussein, A., Hudobivnik, B., Wriggers, P., 2020. A combined adaptive phase field and discrete cutting method for the prediction of crack paths. Computer Methods in Applied Mechanics and Engineering 372, 113329.

[47] Hutchinson, J.W., Suo, Z., 1991. Mixed mode cracking in layered materials. Advances in applied mechanics 29, 63–191.

[48] Ismail, Y., Yang, D., Ye, J., 2016. Discrete element method for generating random fibre distributions in micromechanical models of fibre reinforced composite laminates. Composites Part B: Engineering 90, 485–492.

[49] Jin, B., Cui, H., Fan, H., 2024. Meso-viscoelastic modeling of solid propellant using xct technology and virtual element method. Composite Structures 329, 117784. doi:https://doi.org/10.1016/j.compstruct.2023.117784.

[50] Kim, H.T., Park, K., 2022. Computed tomography (ct) image-based analysis of concrete microstructure using virtual element method. Composite Structures 299, 115937. doi:https://doi.org/10.1016/j.compstruct.2022.115937.

[51] Kuhn, C., Schlüter, A., Müller, R., 2015. On degradation functions in phase field fracture models. Computational Materials Science 108, 374–384.

[52] Kumar, S., Wardle, B.L., Arif, M.F., 2017. Strength and performance enhancement of bonded joints by spatial tailoring of adhesive compliance via 3d printing. ACS applied materials & interfaces 9, 884–891.

[53] Le, B.D., Dau, F., Charles, J.L., Iordanoff, I., 2016. Modeling damages and cracks growth in composite with a 3d discrete element method. Composites Part B: Engineering 91, 615–630.

[54] Li, G., Yin, B., Zhang, L., Liew, K., 2020. Modeling microfracture evolution in heterogeneous composites: A coupled cohesive phase-field model. Journal of the Mechanics and Physics of Solids 142, 103968.

[55] Li, W., Nguyen-Thanh, N., Zhou, K., 2022. Phase-field modeling of interfacial debonding in multi-phase materials via an adaptive isogeometric-meshfree approach. Engineering Fracture Mechanics 269, 108481.

[56] Li, X., Ma, D., Liu, H., Tan, W., Gong, X., Zhang, C., Li, Y., 2019. Assessment of failure criteria and damage evolution methods for composite laminates under low-velocity impact. Composite structures 207, 727–739.

[57] Liu, C., Gong, Y., Gong, Y., Li, W., Liu, Z., Hu, N., 2022. Mode ii fatigue delamination behaviour of composite multidirectional laminates and the stress ratio effect. Engineering Fracture Mechanics 264, 108321.

[58] Liu, G., Dai, K., Nguyen, T., 2007. A smoothed finite element method for mechanics problems. Computational Mechanics 39, 859–877.

[59] Lo Cascio, M., Milazzo, A., Benedetti, I., 2020. Virtual element method for computational homogenization of composite and heterogeneous materials. Composite Structures 232, 111523. doi:https://doi.org/10.1016/j.compstruct.2019.111523.

[60] Maheo, L., Dau, F., Andre, D., Charles, J.L., Iordanoff, I., 2015. A promising way to model cracks in composite using discrete element method. Composites Part B: Engineering 71, 193–202.

[61] Marino, M., Hudobivnik, B., Wriggers, P., 2019. Computational homogenization of polycrystalline materials with the virtual element method. Computer Methods in Applied Mechanics and Engineering 355, 349–372. doi:https://doi.org/10.1016/j.cma.2019.06.004.

[62] Mengolini, M., Benedetto, M.F., Aragón, A.M., 2019. An engineering perspective to the virtual element method and its interplay with the standard finite element method. Computer Methods in Applied Mechanics and Engineering 350, 995–1023.

[63] Miehe, C., Hofacker, M., Welschinger, F., 2010a. A phase field model for rate-independent crack propagation: Robust algorithmic implementation based on operator splits. Computer Methods in Applied Mechanics and Engineering 199, 2765–2778.

[64] Miehe, C., Welschinger, F., Hofacker, M., 2010b. Thermodynamically consistent phase-field models of fracture: Variational principles and multi-field fe implementations. International journal for numerical methods in engineering 83, 1273–1311.

[65] Molnár, G., Gravouil, A., 2017. 2d and 3d abaqus implementation of a robust staggered phase-field solution for modeling brittle fracture. Finite Elements in Analysis and Design 130, 27–38.

[66] Najmeddine, A., Gupta, S., Moini, R., 2025. Coupled large deformation phase-field and cohesive zone model for crack propagation in hard-soft multi-materials. Journal of the Mechanics and Physics of Solids 196, 106016.

[67] Needleman, A., 1987. A continuum model for void nucleation by inclusion debonding. Journal of Applied Mechanics 54, 525–531.

[68] Needleman, A., 1990. An analysis of tensile decohesion along an interface. Journal of the Mechanics and Physics of Solids 38, 289–324.

[69] Needleman, A., 1992. Micromechanical modelling of interfacial decohesion. Ultramicroscopy 40, 203–214. doi:10.1016/0304-3991(92)90117-3.

[70] Nguyen, T.T., Yvonnet, J., Zhu, Q.Z., Bornert, M., Chateau, C., 2016. A phase-field method for computational modeling of interfacial damage interacting with crack propagation in realistic microstructures obtained by microtomography. Computer Methods in Applied Mechanics and Engineering 312, 567–595.

[71] Nguyen-Thanh, N., Li, W., Zhang, Q., Zhou, K., 2025. A hybrid phase-field model for dynamic fracture in fiber-reinforced composites considering interfacial debonding. Computer Methods in Applied Mechanics and Engineering 444, 118110.

[72] Nguyen-Thanh, N., Rabczuk, T., 2024. Phase-field modeling of anisotropic crack propagation based on higher-order nonlocal operator theory. International Journal of Solids and Structures 289, 112632.

[73] Nguyen-Thanh, N., Zhang, Q., Li, W., Wu, M.S., Li, S., Zhou, K., 2023. Higher-order nonlocal operator theory for phase-field modeling of ductile fracture in elasto-plastic materials. Computer Methods in Applied Mechanics and Engineering 414, 116054.

[74] Ortiz, M., Pandolfi, A., 1999. Finite-deformation irreversible cohesive elements for three-dimensional crack-propagation analysis. International journal for numerical methods in engineering 44, 1267–1282.

[75] Paggi, M., Reinoso, J., 2017. Revisiting the problem of a crack impinging on an interface: a modeling framework for the interaction between the phase field approach for brittle fracture and the interface cohesive zone model. Computer Methods in Applied Mechanics and Engineering 321, 145–172.

[76] París, F., Correa, E., Mantič, V., 2006. Kinking of transversal interface cracks between fiber and matrix. Journal of Applied Mechanics 74, 703–716. doi:10.1115/1.2711220.

[77] Park, K., Paulino, G.H., 2011. Cohesive zone models: a critical review of traction-separation relationships across fracture surfaces. Applied Mechanics Reviews 64, 060802.

[78] Park, K., Paulino, G.H., 2012. Computational implementation of the ppr potential-based cohesive model in abaqus: Educational perspective. Engineering fracture mechanics 93, 239–262.

[79] Park, K., Paulino, G.H., Roesler, J.R., 2009. A unified potential-based cohesive model of mixed-mode fracture. Journal of the Mechanics and Physics of Solids 57, 891–908.

[80] Pingaro, M., De Bellis, M.L., Trovalusci, P., Masiani, R., 2021. Statistical homogenization of polycrystal composite materials with thin interfaces using virtual element method. Composite Structures 264, 113741. doi:https://doi.org/10.1016/j.compstruct.2021.113741.

[81] Ren, X., Dai, Y., Dong, Z., Jia, B., Zhao, M., Huang, H., 2025. Mechanical property and failure characteristic of cfrp composite bolted structure ranging from-55° c to 150° c. Thin-Walled Structures , 113787.

[82] Rivarola, F.L., Labanda, N., Benedetto, M., Etse, G., 2020. A virtual element and interface based concurrent multiscale method for failure analysis of quasi brittle heterogeneous composites. Computers & Structures 239, 106338.

[83] Russ, J., Slesarenko, V., Rudykh, S., Waisman, H., 2020. Rupture of 3d-printed hyperelastic composites: Experiments and phase field fracture modeling. Journal of the Mechanics and Physics of Solids 140, 103941.

[84] Shabani, P., Li, L., Laliberte, J., Qi, G., Rapking, D., Mollenhauer, D., 2023. High-fidelity simulation of low-velocity impact damage in fiber-reinforced composite laminates using integrated discrete and continuum damage models. Composite Structures 313, 116910.

[85] Sharma, S., Himanshu, Ramaswamy, A., 2025. Fine to coarse mesh transition in phase-field fracture simulations using the virtual element method. Finite Elements in Analysis and Design 249, 104371. doi:https://doi.org/10.1016/j.finel.2025.104371.

[86] Spada, A., Puccia, M., Sacco, E., Giambanco, G., 2025. A coupled fem-vem approach for crack tracking in quasi-brittle materials. Computer Methods in Applied Mechanics and Engineering 437, 117756. doi:https://doi.org/10.1016/j.cma.2025.117756.

[87] Sreekumar, A., Triantafyllou, S.P., Bécot, F.X., Chevillotte, F., 2020. A multiscale virtual element method for the analysis of heterogeneous media. International Journal for Numerical Methods in Engineering 121, 1791–1821. doi:https://doi.org/10.1002/nme.6287.

[88] Sukumar, N., Bolander, J.E., 2022. Virtual element method for modeling the deformation of multiphase composites. Mechanics Research Communications 124, 103907.

[89] Sukumar, N., Huang, Z., Prévost, J.H., Suo, Z., 2004. Partition of unity enrichment for bimaterial interface cracks. International journal for numerical methods in engineering 59, 1075–1102.

[90] Sukumar, N., Tabarraei, A., 2004. Conforming polygonal finite elements. International Journal for Numerical Methods in Engineering 61, 2045–2066.

[91] Sukumar, N., Tupek, M.R., 2022. Virtual elements on agglomerated finite elements to increase the critical time step in elastodynamic simulations. International Journal for Numerical Methods in Engineering 123, 4702–4725.

[92] Tabarraei, A., Sukumar, N., 2005. Adaptive computations on conforming quadtree meshes. Finite elements in Analysis and Design 41, 686–702.

[93] Talamini, B., Mao, Y., Anand, L., 2018. Progressive damage and rupture in polymers. Journal of the Mechanics and Physics of Solids 111, 434–457.

[94] Tan, W., Martínez-Pañeda, E., 2021. Phase field predictions of microscopic fracture and r-curve behaviour of fibre-reinforced composites. Composites Science and Technology 202, 108539.

[95] Tan, W., Martinez-Paneda, E., 2022. Phase field fracture predictions of microscopic bridging behaviour of composite materials. Composite Structures 286, 115242.

[96] Tarafder, P., Dan, S., Ghosh, S., 2020. Finite deformation cohesive zone phase field model for crack propagation in multi-phase microstructures. Computational Mechanics 66, 723–743.

[97] Tay, T., Sun, X., Tan, V., 2014. Recent efforts toward modeling interactions of matrix cracks and delaminations: an integrated xfem-ce approach. Advanced Composite Materials 23, 391–408.

[98] Turon, A., Davila, C.G., Camanho, P.P., Costa, J., 2007. An engineering solution for mesh size effects in the simulation of delamination using cohesive zone models. Engineering fracture mechanics 74, 1665–1682.

[99] Beirão da Veiga, L., Brezzi, F., Cangiani, A., Manzini, G., Marini, L.D., Russo, A., 2013. Basic principles of virtual element methods. Mathematical Models and Methods in Applied Sciences 23, 199–214.

[100] Beirão da Veiga, L., Brezzi, F., Marini, L.D., Russo, A., 2014. The hitchhiker's guide to the virtual element method. Mathematical models and methods in applied sciences 24, 1541–1573.

[101] Beirão da Veiga, L., Brezzi, F., Marini, L.D., Russo, A., 2016. Virtual element method for general second-order elliptic problems on polygonal meshes. Mathematical Models and Methods in Applied Sciences 26, 729–750.

[102] Vellwock, A.E., Libonati, F., 2024. Xfem for composites, biological, and bioinspired materials: A review. Materials 17. doi:10.3390/ma17030745.

[103] Vodička, R., 2023. A mixed-mode dependent interface and phase-field damage model for solids with inhomogeneities. Theoretical and Applied Fracture Mechanics 127, 104009.

[104] Wang, R., Liu, Y., Mao, J., Liu, Z., Hu, D., 2022. Cyclic cohesive zone model damage parameter acquisition for fatigue crack growth considering crack closure effect. International Journal of Fatigue 163, 107021.

[105] Wei, C., Wu, C., Wojnar, C., 2019. Effect of patterned inclusions on the fracture behavior of ceramic composites. Composites Part B: Engineering 172, 564–592.

[106] Xing, C., Yu, T., Sun, Y., Wang, Y., 2023. An adaptive phase-field model with variable-node elements for fracture of hyperelastic materials at large deformations. Engineering Fracture Mechanics 281, 109115.

[107] Xu, B.B., Peng, F., Junker, P., Wriggers, P., 2025. Virtual element method with non-matching and adaptive meshes for phase field fracture. Computational Mechanics , 1–14.

[108] Xu, S., He, S., Li, J., Xiao, B., Zhang, W., 2023. A progressive damage model for quasi-static tension of 2d woven composites and fem implementation. Composite Structures 320, 117168.

[109] Xu, X.P., Needleman, A., 1993. Void nucleation by inclusion debonding in a crystal matrix. Modelling and Simulation in Materials Science and engineering 1, 111.

[110] Yan, J., Dong, Z., Jia, B., Zhu, S., Li, G., Zheng, Y., Huang, H., 2024. Thermal-mechanical coupling performance of heat-resistant, high-strength and printable al-si alloy antisymmetric lattice structure. Advanced Science 11, 2407107.

[111] Yu, Y., Hou, C., Zhao, M., 2025. A unified anisotropic phase field model for progressive failure of fiber-reinforced composite materials. Journal of the Mechanics and Physics of Solids , 106063.

[112] Zambrano, J., Toro, S., Sánchez, P., Duda, F., Méndez, C., Huespe, A., 2022. Interaction analysis between a propagating crack and an interface: Phase field and cohesive surface models. International Journal of Plasticity , 103341doi:10.1016/J.IJPLAS.2022.103341.

[113] Zhang, D., Zheng, X., Wu, T., 2019. Damage characteristics of open-hole laminated composites subjected to longitudinal loads. Composite Structures 230, 111474.

[114] Zhang, P., Feng, Y., Bui, T.Q., Hu, X., Yao, W., 2020. Modelling distinct failure mechanisms in composite materials by a combined phase field method. Composite Structures 232, 111551.

[115] Zhao, L., Wang, Y., Zhang, J., Gong, Y., Hu, N., Li, N., 2017. Xfem-based model for simulating zigzag delamination growth in laminated composites under mode i loading. Composite Structures 160, 1155–1162.

[116] Zhao, L., Zhi, J., Zhang, J., Liu, Z., Hu, N., 2016. Xfem simulation of delamination in composite laminates. Composites Part A: Applied Science and Manufacturing 80, 61–71.